



# A GPU-Accelerated ray-tracing method for determining radiation view factors in multi-junction thermoelectric generators

Asher J. Hancock <sup>a</sup>, Laura B. Fulton <sup>b</sup>, Justin Ying <sup>c</sup>, Corey E. Clifford <sup>d</sup>, Shervin Sammak <sup>e</sup>, Matthew M. Barry <sup>a,\*</sup>

<sup>a</sup> Department of Mechanical Engineering and Materials Science, University of Pittsburgh, Pittsburgh, PA, 15261, USA

<sup>b</sup> School of Computer Science, Carnegie Mellon University, Pittsburgh, PA, 15213, USA

<sup>c</sup> Department of Computer Engineering, University of Pittsburgh, Pittsburgh, PA, 15261, USA

<sup>d</sup> Department of Nuclear Engineering, Texas A&M University, College Station, TX, 77843, USA

<sup>e</sup> Center for Research Computing, University of Pittsburgh, Pittsburgh, PA, 15213, USA

## ARTICLE INFO

### Article history:

Received 3 September 2020

Received in revised form

4 February 2021

Accepted 18 March 2021

Available online 29 March 2021

### Keywords:

GPU-Accelerated computing

Radiation heat transfer

Ray-tracing

Thermoelectric generator

View factor

## ABSTRACT

A robust computational framework was developed and implemented to numerically resolve the radiation view factor,  $F_{ij}$ , within three-dimensional geometries, and, in particular, thermoelectric generators (TEGs). The proposed numerical methodology utilizes a graphics processing unit-accelerated ray-tracing algorithm to capitalize on the parallel nature of the view factor formulation. The shadow effect, resulting from interference with the TEGs conductive interconnectors and thermoelectric legs, was accounted for via the Möller-Trumbore ray-triangle intersection algorithm with back-face culling enabled. The effect of interconnector thickness, thermoelectric leg height-to-width ratios, TEG packing density, and the number of junctions on  $F_{ij}$  is explored for various TEG configurations. Validation is performed against analytical values for planar and non-planar geometries, in addition to a point-in-polygon intersection algorithm for single-junction TEGs. Results indicate that for a constant packing density,  $F_{ij}$  asymptotically decreases with increasing distance across the TEG's hot- and cold-sides. For an increasing packing density and constant distance across the TEG's junction,  $F_{ij}$  decreases. In a multi-junction device,  $F_{ij}$  was found to asymptotically increase with junction number, implying that for large multi-junction TEG designs, a simpler model may serve to accurately predict the view factor. The code developed herein is open-source and can be found at <https://github.com/AasherH/GPU-Accelerated-View-Factor-Calculator>.

© 2021 Elsevier Ltd. All rights reserved.

## 1. Introduction

Thermoelectric generators (TEGs) are solid-state power generation devices constructed of p- and n-type semiconducting thermoelectric (TE) modules which convert thermal energy directly into electricity via an applied temperature gradient. Fundamentally, TEGs are comprised of coupled TE modules, which are serially linked via highly conductive interconnecting elements. With the application of a thermal differential between a heat source and sink (in a parallel fashion), a voltage potential develops as a result of the Seebeck effect [1].

The benefits of using TEGs for power generation are numerous. With no moving parts or working fluid, TEGs require minimal maintenance, providing reduced operational costs relative to alternative technologies. Furthermore, TEGs are compact, allowing for operation in situations where power is needed but space is limited. Such a situation is well exemplified by the use of radioisotope thermoelectric generators (RTGs) in deep-space power generation systems. Here, the RTGs can supply a steady source of electrical power while the excess heat can keep mission-critical components functional [2,3]. Additionally, TEGs boast a long lifespan, remaining functional for decades after their instantiation. For these reasons, TEGs show tremendous promise for power generation in space exploration, waste heat recovery, and microelectromechanical systems [1,4]. However, despite the advantages offered by TEGs over conventional power generation methods, they have failed to achieve wide-spread commercial use due to their low efficiency, which is often restricted to the 5–15% range [5].

\* Corresponding author.

E-mail addresses: [ajh172@pitt.edu](mailto:ajh172@pitt.edu) (A.J. Hancock), [lfulton@andrew.cmu.edu](mailto:lfulton@andrew.cmu.edu) (L.B. Fulton), [juy20@pitt.edu](mailto:juy20@pitt.edu) (J. Ying), [cec49@tamu.edu](mailto:cec49@tamu.edu) (C.E. Clifford), [shervin.sammak@pitt.edu](mailto:shervin.sammak@pitt.edu) (S. Sammak), [matthew.michael.barry@pitt.edu](mailto:matthew.michael.barry@pitt.edu) (M.M. Barry).

<b>Nomenclature</b>	
<i>Variables</i>	
A	Surface area or Point, m <sup>2</sup>
B, C	Point
BA, CA	Edge
dF <sub>ij</sub>	Differential radiation view factor, dimensionless
D	Normalized direction or Spatial dimension
F	View factor matrix
F <sub>ij</sub>	Radiation view factor, dimensionless
FS	Factor of safety
H	Height, m
I	Identity matrix
$\vec{n}$	Unit normal vector
N	Number of junctions
O	Origin
PF	Power factor, V <sup>2</sup> K <sup>-2</sup> Ω <sup>-1</sup> m <sup>-1</sup>
Q <sub>i</sub>	Radiation heat transfer rate, W
$\vec{R}$	Radiative ray vector
T	Temperature or Edge, K
u, v	Scalar
t	Thickness or Distance, m
W	Width, m
W <sub>G</sub>	Gap width, m
X, Y, Z	Vertex
ZT	Thermoelectric figure of merit, dimensionless
<i>Greek symbols</i>	
$\alpha$	Seebeck coefficient, VK <sup>-1</sup>
$\epsilon$	Emissivity, dimensionless
<i>Subscripts</i>	
c	Corrected
el	Electrical
i	Emitting surface
int	Interconnector
j	Receiving surface
N	N-type
o	Original
P	P-type
s	Spatial
T	Total
<i>Acronyms</i>	
Avg	Average
CAD	Computer-aided design
CL	Computing language
CPU	Central processing unit
Diff	Difference
GPU	Graphics processing unit
MT	Möller-Trumbore
RTG	Radioisotope thermoelectric generator
STL	Stereolithography file
TEG	Thermoelectric generator
TE	Thermoelectric
Tess	Tessellations

TEG performance depends upon the device design and the selection of thermoelectric material, which is partially dictated by the operating differential between the heat source and sink. To harness the Seebeck effect, a sufficient temperature difference must be applied across the p-n junction, which necessitates consideration of geometrical factors and their relation to device performance. At the same time, analysis of the thermoelectric material properties, in relation to the established temperature gradient and heat transfer characteristics, is vital for achieving maximum conversion efficiency or maximum power output [1,6]. Thus, developing the next generation of TEGs which improve upon the current working efficiencies is dependent upon a holistic approach that couples device design optimization and material performance [7].

Thermoelectric material performance is primarily characterized by the dimensionless figure of merit, ZT,

$$ZT = \frac{\alpha^2 \sigma_{el} T}{\kappa} = \frac{PF}{\kappa} \bar{T} \quad (1)$$

which is a function of  $\alpha$ , the Seebeck coefficient,  $\sigma_{el}$ , the electrical conductivity,  $\kappa$ , the thermal conductivity, and  $\bar{T}$ , the average absolute temperature across the TEG junction. The numerator of the third term within this expression, PF, is referred to as the power factor, which equates to  $\alpha^2 \sigma_{el}$ . For nearly half a century, ZT for commercially available thermoelectrics has remained near 1, whereas for TEGs to be competitive with current energy-generation technologies, a ZT value of at least 3–4 is needed [8,9].

A large power factor signifies an efficient heat-to-electricity conversion, while a low thermal conductivity is necessary to

maintain the appropriate temperature gradient across the p-n junction [10]. Ideal TE materials possess a large Seebeck coefficient and electrical conductivity but a small thermal conductivity — challenging requirements given the adverse relationship of these properties in traditional thermoelectric materials. However, despite the nonlinear and interdependent relationship of the properties comprising Equation (1), recent efforts have made great strides in raising ZT. For example, Pei et al. [11,12] achieved a thermoelectric figure of merit of 1.8 by fine-tuning the carrier concentrations in PbTe<sub>1-x</sub>Se<sub>x</sub> alloys to achieve high valley degeneracy and an increased density-of-state effective mass without reducing the carrier mobility. Moreover, alloying p-type PbTe with MnTe demonstrated an improved figure of merit for small temperature gradients while enhancing alloy scattering effects at higher temperatures, ultimately leading to an enhanced ZT. Likewise, others have achieved thermoelectric material enhancement through the utilization of doping and alloying to achieve more favorable electronic band structures [13,14]. Zhang et al. [15] found that n-type PbSe, doped with Al, could increase the Seebeck coefficient by increasing the local density of states near the Fermi level. Furthermore, the microstructures created in the Al:PbSe served to intensify phonon scattering and decrease the thermal conductivity. Improvements in thermoelectric materials have also been accomplished via nano-structuring and nano-fabrication techniques to control multi-length phonon scattering. One such example is how Zhu et al. [16] utilized nanostructured silicon, with grain and point defects, and found that the thermal conductivity decreased by a factor of ten. Additionally, there are numerous comprehensive reviews on the material improvements of thermoelectric materials

[17–19].

On the other hand, a TEG's geometry must be taken into account to maximize thermal-to-electric conversion. Device performance is a function of a variety of geometrical parameters including thermoelectric material height and width, interconnector thickness, and packing density [20]. These parameters directly affect the device working conditions, such as the maximum obtainable temperature gradient, and thus affect the ultimate thermal efficiency. For example, Kim et al. [21] found that shorter thermoelectric legs are favorable for large power outputs. However, the induced thermal stresses on TEG designs with shorter legs could be too great from a thermo-mechanical perspective. Therefore, a balance between thermoelectric performance and device reliability must be observed.

Since the thermoelectric material properties listed in Equation (1) are dependent upon temperature and are interdependent amongst themselves, a maximum  $Z\bar{T}$  is usually obtainable within a specific temperature range [22]. Consequently, recent studies have focused on developing TEGs to endure the required temperature gradient while maintaining favorable thermoelectric properties. Using ANSYS Fluent, Shu et al. [23] developed a three-dimensional model of a TEG with a segmented structure to match the temperature gradient in the radial direction; results indicated an increased maximum power output in comparison to an ordinary structure. Tian et al. [24] created a mathematical model of a segmented TEG (with varying thermocouple lengths) as a waste heat recovery device and found that given an adjusted thermoelectric material ratio, optimal performance is achieved with an increased heat source temperature and a decreased heat sink temperature.

If high-grade thermoelectric generators are operated at high temperatures, it is imperative that the analytical models developed accurately represent the underlying heat transfer phenomena. For instance, as the magnitude of the temperature gradient increases, heat transfer becomes increasingly radiation-dominant due to the quartic dependence on temperature. However, while the analysis of conduction and convection are commonly integrated within thermoelectric device studies, radiation often remains ignored or oversimplified due to the challenges associated with calculating the radiation view factor. While numerous studies have worked to resolve the view factor in a tractable manner, most have fallen short of ubiquity through either narrow applicability or computational intensity.

### 1.1. Literature review of view factor calculations

Recent numerical methodologies have focused on using ray-tracing, in combination with the Monte Carlo method, to resolve the radiation view factor. One of the first instances of utilizing this combined methodology is attributed to Argento and Bouvard [25], who used it to evaluate radiative heat transfer properties in porous media. Following this development, many other researchers have published work to expand upon the combined ray-tracing and Monte Carlo scheme.

Vujičić et al. [26] combined the Monte Carlo method with the finite element technique to resolve the view factors between two parallel plates; here, it was found that an increased mesh density paradoxically decreased numerical accuracy, a result stemming from the stochastic nature of the Monte Carlo method. Furthermore, the authors note that as the number of rays per element increases, the processing time may quickly become computationally infeasible. Walker et al. [27] presented a Monte Carlo governed ray-tracing algorithm to analyze the view factors within an operational fiber drawing furnace. While they found that the model setup time is independent of geometric complexity, they stated that

the computational run times are longer in comparison to numerical integration schemes. Cremona et al. [28] studied the influence of misalignment on the radiative view factors between a sample and a cone calorimeter via the Monte Carlo method. While decent results were observed, statistically large errors intrinsic to the Monte Carlo method [29] unfortunately led to statistically large errors in the view factor (approximately 5% for the relative standard deviation of view factor values). Mirhosseini et al. [30] utilized the Monte Carlo method to resolve the view factors within a solar chimney power plant and concluded that the Monte Carlo method provided more accurate values in comparison to the analytical solutions available. However, the authors again noted the trade-off between numerical resolution and computational volume. Vilchez et al. [31] devised a numerical ray-tracing algorithm to resolve the view factors between a chemical fireball (a spherical surface) and a target surface with an obstructive surface in-between. While successful results were obtained for this specific configuration, this work is unfortunately only relevant for view factors concerning a sphere and a differential area; hence, it is limited in applicability to more complex geometries.

Other noteworthy studies utilized more rigorous mathematical formulations to calculate the view factor. Feng et al. [32] worked to evaluate the geometric view factors within randomly packed beds of equally sized spheres for modeling the radiative heat transfer within high-temperature pebble-bed nuclear reactors. While their use of the Tanaka integral and Fibonacci integration scheme proved effective for small pebble-bed reactor assemblies, they noted the substantial central processing unit (CPU) computational costs required to simulate large-scale reactor models. Vorre et al. [33] resolved the view factors between bystanders and large buildings for building energy simulations. Their methodology utilized numerical integration, specifically Simpson's rule, on projected area factors by simplifying complex geometries into a set of primitive shapes. While this method yielded quick run times, in comparison to the computationally expensive ray-tracing method, it yielded low accuracy. Narayanaswamy [34] derived an analytical expression for the radiative view factor between two arbitrarily oriented planar triangles via Nusselt's unit sphere method. This method averts the use of numerical quadrature and preserves the reciprocity of the view factor calculation; additionally, the expression is valid for clockwise and counterclockwise vertex ordering. However, like the work of Vilchez et al. [31], this method is only valid for planar surfaces and is limited in generality. Sönmez et al. [35] proposed a view factor estimation method that utilized ray casting and the Fibonacci lattice technique to analyze photovoltaic modules in a three-dimensional environment. When comparing the numerical sky view factor to the experimentally determined value, an average error of 3.82% was observed. Therefore, depending upon the complexity of the environment and the accuracy required, this method may lack sufficient geometric resolution.

One of the enduring computational challenges with calculating the view factor is the accurate and efficient handling of geometries featuring obstructions (blocked participating surfaces), and numerous studies have worked to solve this problem. Walton utilized a projection method to detect potential obstructions, in tandem with adaptive integration and convex subdivision techniques, to calculate the view factor between two surfaces. However, it was noted that in certain geometrical configurations, where the projection of the nonparticipating surface is off-centered, erroneous view factor calculations can be made [36]. A significant study conducted by Kramer et al. [37] employed an OpenGL framework to calculate obstructed area-to-area view factors. Harnessing GPU-computing, they achieved low computational runtimes via Gaussian quadrature and a hemicube method in warehouse and test cabin configurations. Mahmood and Hu [38] developed a program

in FORTRAN-90 to evaluate the view factors between unobstructed and obstructed square enclosures via the crossed-strings method. However, they discuss notable differences between their calculated values and those predicted by the summation rule for closed cavities when multiple obstructions are present.

## 1.2. Motivation

While there are view factor calculation methods for specific situations, it is clear there is a demand for an efficient and robust procedure to calculate the radiation view factor within complex geometries. In this study, the proposed numerical methodology rapidly calculates  $F_{ij}$  within TEGs via graphics processing unit (GPU)-accelerated programming. Specifically, the current study focuses on determining the view factor between the hot- and cold-side ceramic plates for the largest observed temperature gradients using an in-house GPU-accelerated ray-tracing program. Said program is able to account for planar and non-planar geometries positioned in any orientation, as well as the shadow effect and self-intersection via the implementation of the Möller-Trumbore (MT) ray-triangle intersection algorithm with back-face culling enabled. The proposed numerical methodology is demonstrated on various TEG geometries and a near two orders of magnitude reduction in computation time, relative to a CPU-based version of the code, is demonstrated while preserving solution accuracy. Thus, a fast, versatile, and accurate method of calculating radiation view factors within complex three-dimensional geometries is demonstrated and provided as an open-source executable Java code.

To explore the effect of various TEG geometrical parameters upon  $F_{ij}$ , the thermoelectric leg height-to-width ratio ( $H/W$ ), interconnector thickness ( $t_{int}$ ), TEG packing density ( $\phi$ ), and number of thermoelectric junctions within the module ( $N$ ) are varied. The impetus for studying the effects of TEG geometry, and specifically the number of junctions, on the value of  $F_{ij}$  arises from the fact that terrestrial TEGs and extra-terrestrial RTGs are comprised of hundreds of uni-couples, which can be viewed as multi-junction TEGs. For instance, the general purpose heat source RTG used within various National Aerospace and Space Administration missions, such as the Galileo, Cassini, and New Horizons missions, was comprised of 572 SiGe junctions surrounding the plutonium-238 heat-source modules [39].

To introduce this GPU-accelerated ray-tracing algorithm, and to demonstrate its efficacy on various TEG design configurations, this work is organized as follows: the mathematics, algorithm development, and solution methodology for calculating the radiation view factor are described in Section 2. The prescribed computational framework is then further elaborated upon and validated against numerous analytical test cases in Section 3, which include planar and non-planar participating surfaces, as well as a single-junction TEG model using alternative algorithms for calculating the view factor. Following numerical validation, Section 4 evaluates and presents the view factor for a variety of thermoelectric generator designs with their corresponding numerical uncertainty. Finally, Section 5 presents a discussion of the results and trends found within this study while Section 6 provides the conclusion and the final remarks.

## 2. Solution methodology

### 2.1. Mathematics

The radiation view factor,  $F_{ij}$ , is purely a geometrical factor that represents the proportion of diffuse radiation emitted by one surface,  $A_i$ , and received by another,  $A_j$ ; it is related to the net radiation

heat transfer rate,  $Q_i$ , between the two participating surfaces by

$$Q_i = \epsilon \sigma A_i F_{ij} (T_i^4 - T_j^4) \quad (2)$$

where  $\epsilon$  represents the emissivity of the material and  $\sigma$  represents the Stefan-Boltzmann constant.

The radiation view factor is calculated as

$$F_{ij} = \frac{1}{A_i} \int_{A_i} \int_{A_j} \frac{\cos(\theta_i) \cos(\theta_j)}{\pi \left\| \vec{R}_{ij} \right\|^2} dA_j dA_i \quad (3)$$

where the numeric resolution of  $F_{ij}$  between two participating surfaces,  $A_i$  and  $A_j$ , is accomplished through discretizing the total area of both surfaces into  $N_i$  and  $N_j$  triangular differential areas, which are hereby denoted as  $dA_i$  and  $dA_j$ , respectively. The radiative ray vector,  $\vec{R}_{ij}$ , is cast from the centroid of one emitting discretization,  $dA_i$ , to the centroid of another receiving discretization,  $dA_j$ . The centroidal coordinates per discretization are defined as

$$X_i = \frac{X_{1i} + X_{2i} + X_{3i}}{3} \quad (4)$$

$$Y_i = \frac{Y_{1i} + Y_{2i} + Y_{3i}}{3} \quad (5)$$

$$Z_i = \frac{Z_{1i} + Z_{2i} + Z_{3i}}{3} \quad (6)$$

where  $X_{1i}$ ,  $Y_{1i}$ , and  $Z_{1i}$  represent the coordinates of the first vertex of the differential area in the Cartesian coordinate system. The polar angles,  $\theta_i$  and  $\theta_j$ , between the unit normal vectors,  $\vec{n}_i$  and  $\vec{n}_j$ , of  $dA_i$  and  $dA_j$ , respectively, are calculated as

$$\theta_{ij} = \cos^{-1} \left( \frac{\vec{n}_{ij} \cdot \vec{R}_{ij}}{\left\| \vec{n}_{ij} \right\| \left\| \vec{R}_{ij} \right\|} \right) \quad (7)$$

**Fig. 1** provides an example of the pertinent variables in

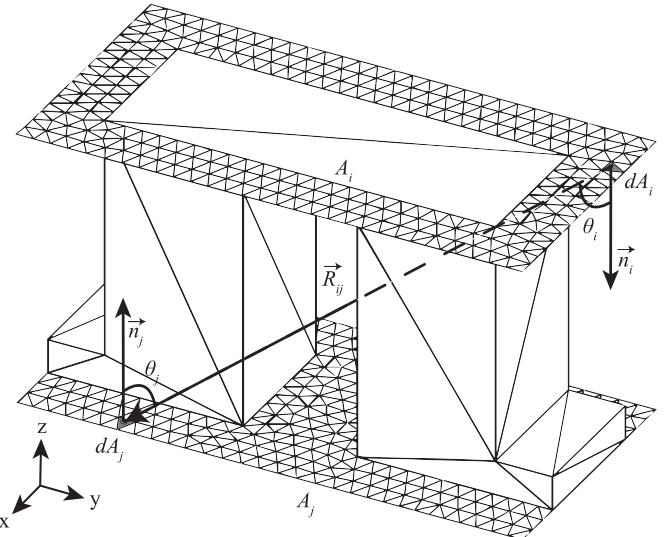


**Fig. 1.** Geometrical parameters when calculating the view factor across a single-junction thermoelectric generator design with  $N = 1$ .

calculating the view factor across a single-junction thermoelectric generator's hot- and cold-side ceramic plates.

To determine the total amount of radiation emitted from one surface and received by another, each differential area contained within  $A_i$  participates with each differential area contained within  $A_j$ ; thus, a summation convention is applied to each contributing view factor such that

$$F_{ij} = \frac{1}{A_i} \sum_{i=1}^{N_i} \sum_{j=1}^{N_j} \frac{\cos(\theta_i) \cos(\theta_j)}{\pi \|\vec{R}_{ij}\|^2} dA_j dA_i. \quad (8)$$

As is evident, the number of rays utilized per view factor calculation corresponds to the product of the number of emitting differential areas,  $dA_i$ , with the number of receiving differential areas,  $dA_j$ .

## 2.2. Shadow effect

The shadow effect is a phenomenon that represents any potential radiative transfer with a non-participating surface, and it is an important consideration when resolving the view factor between two bodies. An example of the shadow effect is presented in Fig. 1; here, the ray emanating from the upper surface is obstructed by the thermoelectric leg (depicted by the dashed line). As illustrated, the ray vector is intercepted by the TE leg and will not contribute to the overall view factor calculation. In this work, the shadow effect was accounted for via the MT ray-triangle intersection algorithm. This intersection algorithm was chosen for its computational efficiency, as it averts the precomputation of the plane equation intrinsic of other triangle intersection algorithms. For the sake of brevity, only the major details of the MT algorithm are described below; interested readers are encouraged to consult [40] for a complete description.

In determining a ray-triangle intersection, the intersection point is represented as a superposition of scalars and vertices written in barycentric coordinates as

$$O + t\vec{D} = (1 - u - v)A + uB + vC \quad (9)$$

where  $O$  represents the origin of the ray,  $\vec{D}$  represents the normalized directional ray vector,  $u$  and  $v$  represent the barycentric

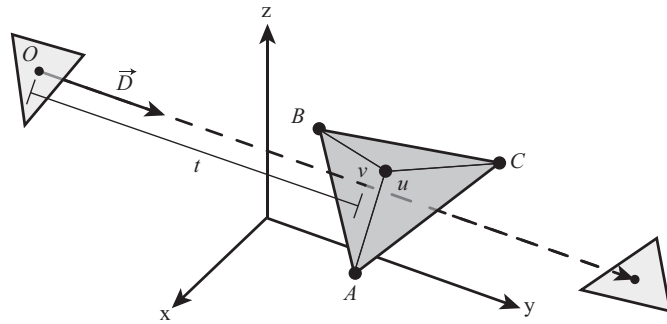


**Fig. 2.** Geometrical setup in the Möller-Trumbore algorithm.

coordinates of the intersecting triangle,  $A$ ,  $B$ , and  $C$ , represent the vertices of the intersecting triangle, and  $t$  represents the distance from the ray's origin to the intersection point (see Fig. 2).

Since barycentric coordinates are intrinsically normalized, the following statements hold for the feasibility of intersection:

$$0 \leq u, v \leq 1 \quad (10)$$

$$0 \leq u + v \leq 1 \quad (11)$$

Rearranging Equation (9) with new variables and writing in matrix form yields

$$\begin{bmatrix} -\vec{D} & \vec{BA} & \vec{CA} \end{bmatrix} \begin{bmatrix} t \\ u \\ v \end{bmatrix} = \vec{T} \quad (12)$$

where  $\vec{BA}$  and  $\vec{CA}$  represent the edges of the intersecting triangle with a shared vertex  $A$  and  $\vec{T}$  represents the translation from the origin  $O$  to vertex  $A$ .

Finally, Cramer's rule is used to solve the above system of equations where the unknowns describing the unit triangle are

$$\begin{bmatrix} t \\ u \\ v \end{bmatrix} = \frac{1}{|-\vec{D} \cdot \vec{BA} \cdot \vec{BC}|} \begin{bmatrix} |\vec{T} \cdot \vec{BA} \cdot \vec{BC}| \\ |-\vec{D} \cdot \vec{T} \cdot \vec{BC}| \\ |-\vec{D} \cdot \vec{BA} \cdot \vec{T}| \end{bmatrix} \quad (13)$$

Equation (13) represents all the logical checks utilized when accounting for the shadow effect within any geometry. Due to the barycentric coordinate definition, if either  $u$  or  $v$  fails the requirement of Equation (10), then it is immediately determined that no intersection exists. Otherwise, if the given ray-triangle combination satisfies Equation (10) and the calculated value of  $t$  equates to less than the original ray's magnitude, an intersection is detected and the algorithm ends its execution.

## 2.3. Domain decomposition

To ensure this view factor methodology maintains ease of use in future thermoelectric generator designs, a robust means of geometry description was sought. Given the ubiquity of stereolithography (STL) files in mechanical design, including the multitude of computer-aided design (CAD) software capable of exporting assemblies in such a file type, all geometry utilized in the following development was defined via STL file format. Depending

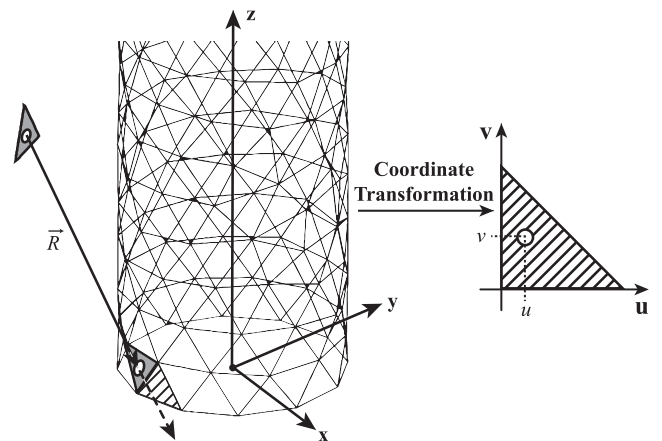


**Fig. 3.** Erroneous intersection detection with culling disabled.

upon the geometry, the emitting, receiving, and any non-participating (blocking) surfaces were discretized using either a modified mesh generator in MATLAB [41] or SolidWorks [42], a prevalent CAD software, to create the tessellations defined within the STL file.

When formulating the view factor, each triangular differential area defined by the participating surface's STL file was found via the vector cross product of the triangle's edges

$$dA_i = \frac{1}{2} \left\| \overrightarrow{BA_i} \times \overrightarrow{CA_i} \right\|. \quad (14)$$

Every differential area of the emitter surface created a corresponding ray for each receiver differential area, where the ray vectors were determined by the centroidal locations of each triangle. These rays, in combination with the triangle's calculated area and corresponding normal vectors, were utilized to populate Equation (3), where the overall summation from each discretization formed the overall view factor between the two surfaces.

The two participating geometries were finely meshed for numerical accuracy, while any non-participating geometry that existed in-between  $A_i$  and  $A_j$  was coarsely meshed to decrease the number of logical checks required by the MT algorithm. For surface discretization, the uniformity of each tessellation's size and distribution within the surface was enforced to accurately depict the geometry under consideration. In addition, all the vertices belonging to each tessellation described within the STL file followed a counter-clockwise winding convention, with respect to the geometry's local Cartesian coordinate system.

#### 2.4. Back-face culling

Back-face culling is a computer graphics technique referring to the removal of primitive geometries that face away from the camera [43]. To determine whether a triangle (face) is culled, consideration of the triangle's orientation, with respect to some other triangle, is necessary. In this work, orientation was determined by a triangle's vertex winding with respect to an observer. Therefore, if all triangles obeyed a counter-clockwise vertex winding convention, then from any given triangle's perspective, culled tessellations appeared clock-wise wound.

Back-face culling was enabled for two primary reasons: it

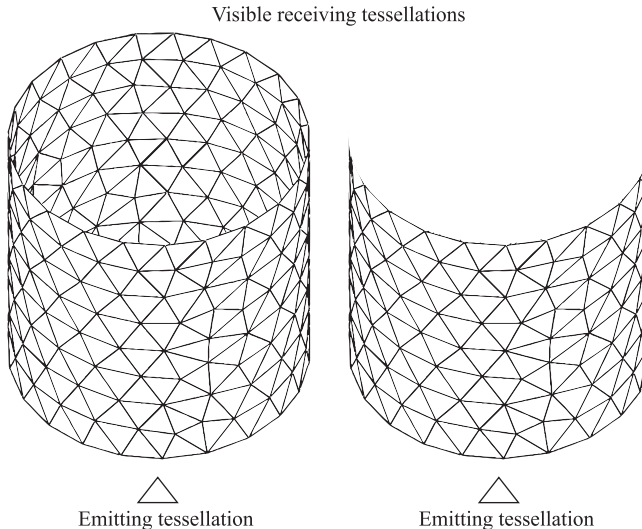


**Fig. 4.** Visible tessellations for ray-casting between the emitter and receiver with (right), and without (left), back-face culling enabled.

increased computational savings and it prevented false-positive intersections. Consider the situation of resolving  $F_{ij}$  within a cylinder of finite length as depicted in Fig. 3. If the radiative directional vector, between the emitting and receiving surfaces, continued onward and passed through the hatched non-participatory tessellation, the calculated scalars from the MT algorithm,  $u$  and  $v$ , satisfy Equation (10). Therefore, the only other scalar that needs to be validated for a positive intersection check is  $t$ . While it is physically impossible for the hatched tessellation to cause an intersection between the depicted  $dA_i$  and  $dA_j$ , it is computationally possible when working with non-planar surfaces. Due to the numerical discretization of the geometry's curvature, the calculated  $t$  value can equate to less than the ray magnitude,  $\|\vec{R}\|$ , thus yielding an erroneous intersection when combined with acceptable  $u$  and  $v$  values. For this reason, merely increasing the surface's mesh density fails to properly resolve  $F_{ij}$  when the curvature is exhibited. Mathematically, this is seen through solving for  $t$  in Equation (13), where

$$t = \frac{-(\overrightarrow{BA} \times \overrightarrow{CA}) \cdot \vec{T}}{(\overrightarrow{BA} \times \overrightarrow{CA}) \cdot \vec{R}} < \|\vec{R}\|. \quad (15)$$

To compensate for this possibility, back-face culling was utilized, which manifested as a sign check on the determinant of the transformation matrix listed in Equation (12): if negative, the triangle under consideration appeared clock-wise wound and was culled, which caused the MT algorithm to stop the execution. Therefore, all culled tessellations were not checked for ray-triangle intersection, thus preserving the correct calculation of  $F_{ij}$ . In consequence, back-face culling offered runtime savings since fewer tessellations required logical checks by the shadow effect routine. Fig. 4 depicts the visible tessellations available for ray-casting with, and without, culling enabled.

### 3. Computational methodology and analytical validation

#### 3.1. GPU-accelerated programming

As previously noted in Section 2.3, a refined mesh was required for an accurate view factor calculation. Accuracy is synonymous with large computational costs due to the proportional growth of

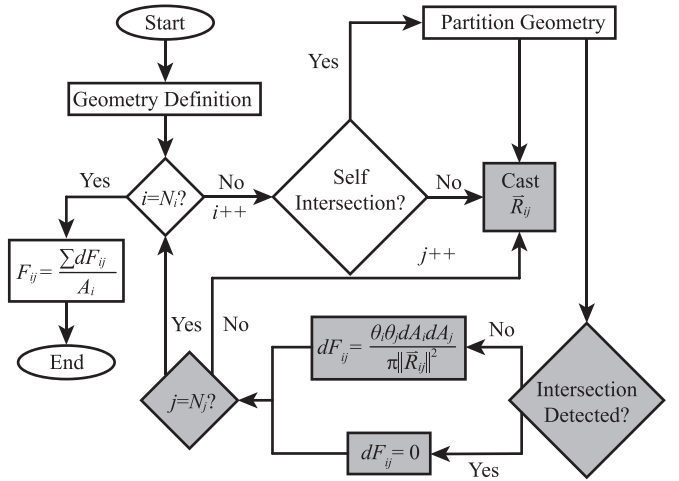


**Fig. 5.** Flow chart of this work's view factor numerical methodology. Processes computed on the device's GPU are highlighted.

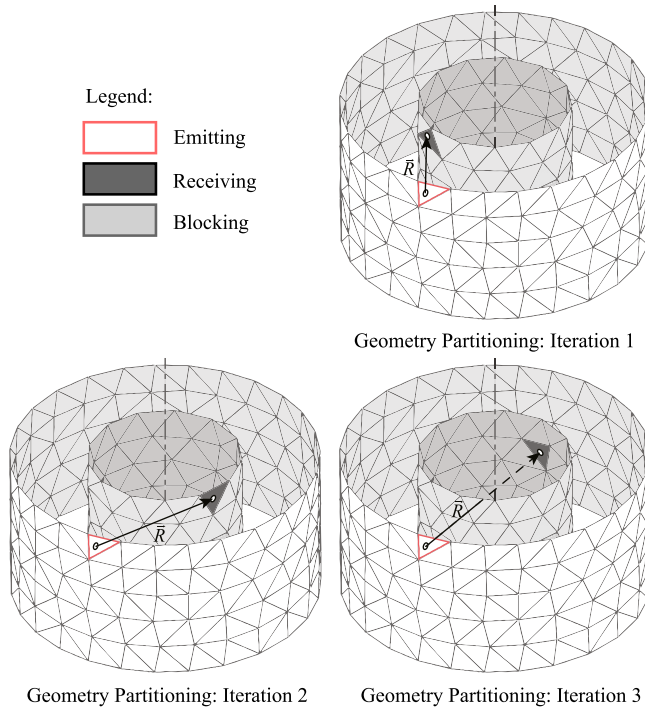


**Fig. 6.** Example geometry partitioning during self-intersection. The receiving geometry is continuously represented as a series of receiving tessellations while the remainder of the original geometry is treated as a non-participating surface.

cast rays with mesh refinement, coupled with the numerous logical checks required by the MT algorithm. Consequently, if computed on a computer's central processing unit (CPU), which typically consists of only a few cores, the view factor's calculation can quickly become intractable.

Graphics processing units (GPUs), on the other hand, consist of hundreds of processing units (cores) and thousands of threads, which can operate in parallel to drastically improve computational performance. While CPUs and GPUs serve different purposes, GPUs are often better suited for repetitive and algebraically intensive tasks. Since the mathematics described in the view factor formulation and MT algorithm routine are purely arithmetical and independent of neighboring elements, the given problem is suitable for GPU-acceleration.

To achieve the computational savings intrinsic of GPU computing, an in-house code was created, in Java, via extensive use of the Aparapi programming library package. Aparapi is an open-source application programming interface for executing native Java code on the GPU, where it works by converting the Java byte code to an Open Computing Language (CL) kernel at runtime [44]. While the use of OpenCL allowed for operation on most commercially available hardware, it presents some programmatical constraints like restricted object referencing and limited use of primitive data types. The aforementioned limitations posed procedural challenges for geometry instantiation upon the graphics processing unit. To navigate any potential parallel execution errors, problem logistics, such as surface definition, tessellation ordering, and geometry precomputation (the calculation of tessellation areas and centroids) were carried out on the CPU, while the time-intensive and repetitive arithmetic operations, such as ray casting and intersection detection, were performed on the GPU.

An overview of the presented computational methodology is described in Fig. 5's flow chart. Once the user has generated the STL files for the corresponding test configuration, the files are separated

into emitting, receiving, and blocking geometries, respectively. The program then instantiates a kernel for every emitting tessellation with a size equal to the number of receiving tessellations. In this manner, every tessellation within the emitting geometry casts a ray to every tessellation within the receiving geometry.

For every cast ray, the MT algorithm checks for an intersection with every surface designated as non-participatory. If an intersection is detected with any non-participating surface, the subsequent ray does not contribute to the overall view factor calculation and the next ray is cast; if no intersection is detected, the view factor, without division of the area scalar, is calculated and stored. This process repeats until all of the cast rays are accounted for, which prompts for the final summation of differential view factors,  $dF_{ij}$ . The final step consists of dividing by the emitting surface's total area, ultimately yielding the final view factor value.

### 3.2. Geometry partitioning

During the geometry definition phase, as shown in Fig. 5, only the pertinent geometrical data for the emitting, receiving, and blocking geometries were passed onto the GPU to decrease memory allocations. This minimizes the potential for data transfer bottlenecks, which allows for greater instances of parallel computation.

As discussed previously, if curved surfaces are run within the view factor calculator, back-face culling can prevent erroneous intersection detection. However, given a case similar to the one represented within Fig. 6, it is possible for the user's defined participating surfaces to create "self-intersections" during the ray casting procedure, even when no explicit blocking geometry is defined; in this work, self-intersections refer to any obstructive tessellations, intrinsic of either emitting or receiving geometries, that need to be checked for possible ray-intersection via the MT algorithm.

As demonstrated in Fig. 6's rightmost configuration, the cast ray must first pass through the receiving surface's convex region. Since no blocking geometries were explicitly assigned, the intersection with the convex surface will not be detected. To account for this internal interference when the view factor between curved bodies is calculated, a self-intersection geometry partitioning algorithm was implemented. Illustrated in Fig. 6 is the workflow undergone when the self-intersection function is called. The obstructive geometry, which could belong to either participating surface, is partitioned into "blocking" arrays for the MT algorithm to check. The blocking array constitutes every tessellation, within either the emitting or receiving geometry, except the current tessellation pair used for ray casting. In this manner, there exists only one tessellation per participating surface at any given time, while the rest of

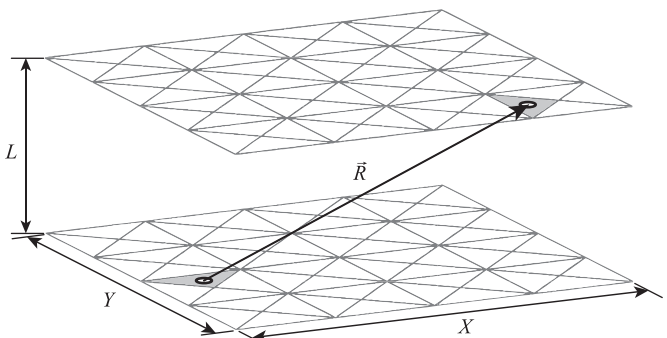


**Fig. 7.** Geometrical depiction of the aligned parallel rectangles validation case.

**Table 1**

Comparison of numerical view factors in aligned parallel rectangles with the analytical solution.

X	Y	Analytic Solution	Numeric Solution	Error [%]
0.1	0.1	3.162056839e-3	3.162056892e-3	1.68e-06
0.2	0.2	1.240397731e-2	1.240397811e-2	6.44e-06
0.4	0.4	4.613741674e-2	4.613742709e-2	2.24e-05
0.6	0.6	9.336233784e-2	9.336237683e-2	4.18e-05
1.0	1.0	1.998248957e-1	1.998250489e-1	7.67e-05
2.0	2.0	4.152532836e-1	4.152538458e-1	1.35e-04
4.0	4.0	6.320364300e-1	6.320378492e-1	2.25e-04
10.0	10.0	8.269945224e-1	8.269984901e-1	4.80e-04

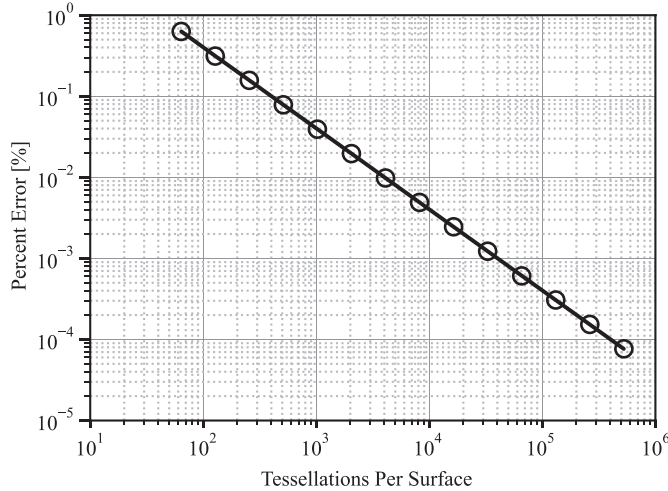


**Fig. 8.** Percent error of aligned parallel rectangles with increasing tessellations for  $X/L$  and  $Y/L = 1.0$ .

the geometry is considered non-participatory. After each iteration through the emitting or receiving geometry, the blocking and participating geometries are partitioned again, a process that repeats until the end of both STL files are reached.

However, given the hybridized architecture described in this geometry partitioning procedure, limited decrements in computation time are achievable. This is because the number of non-participatory surfaces grows proportionally with mesh refinement, resulting in greater intersection checks by the MT algorithm. While there exist many factors that can affect the efficiency of GPU-

acceleration, it was found that if the number of tessellations within the blocking array surpassed roughly ten thousand, runtimes reached exorbitant amounts. Therefore, within this methodology, the authors recommend limiting curved geometries because the self-intersection algorithm can prove too computationally demanding for some high-fidelity models. This issue could potentially be alleviated by extending the algorithm and subsequent code to multi-GPU acceleration. Regardless, to the authors' best knowledge, the methodology described in this work is one of the most robust, efficient, and readily engineering design-compatible programs available in the literature.

### 3.3. Model validation

#### 3.3.1. Comparison to analytic

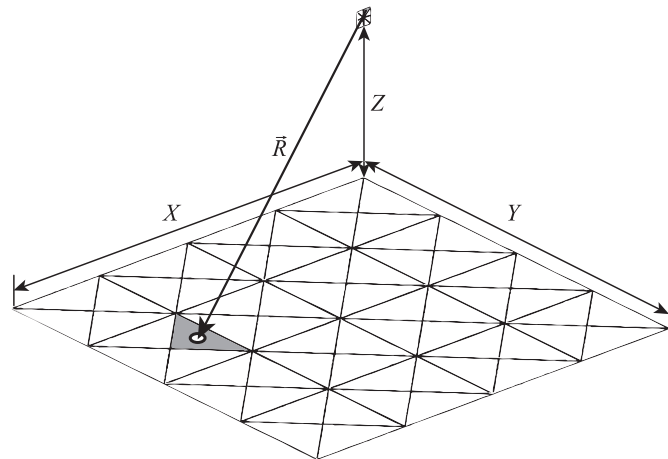
The following subsections provide a basis for validating the proposed view factor calculation methodology. First, the program was subjected to a variety of primitive geometrical inputs commonly encountered within thermoelectric generator designs. One example includes parallel surfaces, which resemble the opposing hot- and cold-side ceramic plates separated across the junction by the inner thermoelectric modules. In these configurations, the MT algorithm does not execute since no explicit blocking geometry in-between the participating surfaces was defined. Consequently, the self-intersection and culling techniques were not utilized either.

Next, to demonstrate robustness in complex models, non-planar geometrical primitives, such as concentric cylinders and spheres, were inputted into the view factor calculator. These geometries required resolution of the shadow effect, which employs the MT and self-intersection algorithms, along with back-face culling. As mentioned previously, view factor validation tests that utilized curved surfaces reported greater runtimes than those calculated in other configurations due to the increased number of logical checks required by the self-intersection algorithm.

**3.3.1.1. Aligned parallel rectangles.** The first primitive geometrical input validated were two parallel rectangular areas. The plates are separated by some distance  $L$ , and have lengths and widths of  $X$  and  $Y$ , respectively (refer to the schematic in Fig. 7). The analytic solution as presented by Ref. [45] requires the calculation of a normalized length and width such that

$$\bar{X} = \frac{X}{L}, \quad \bar{Y} = \frac{Y}{L}. \quad (16)$$

The value of  $F_{ij}$  based upon  $\bar{X}$  and  $\bar{Y}$  is given as

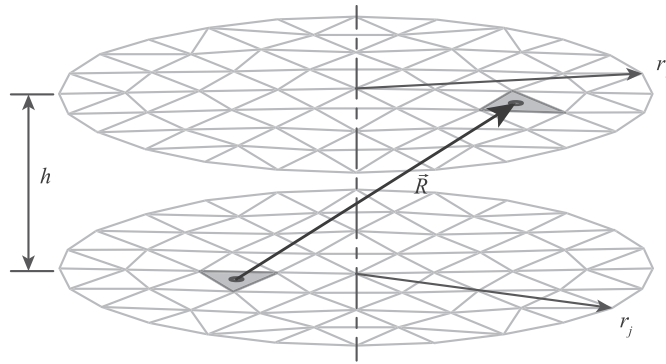
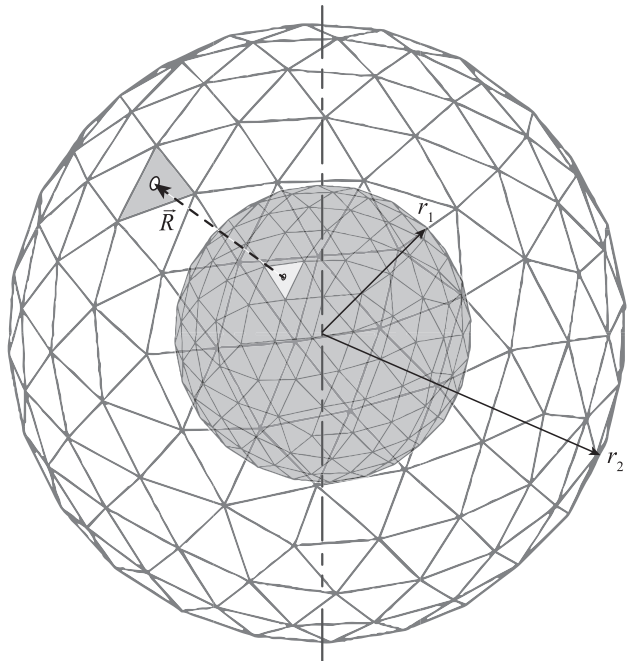


**Fig. 9.** Geometrical depiction of the perpendicular plates with a differential area validation case.

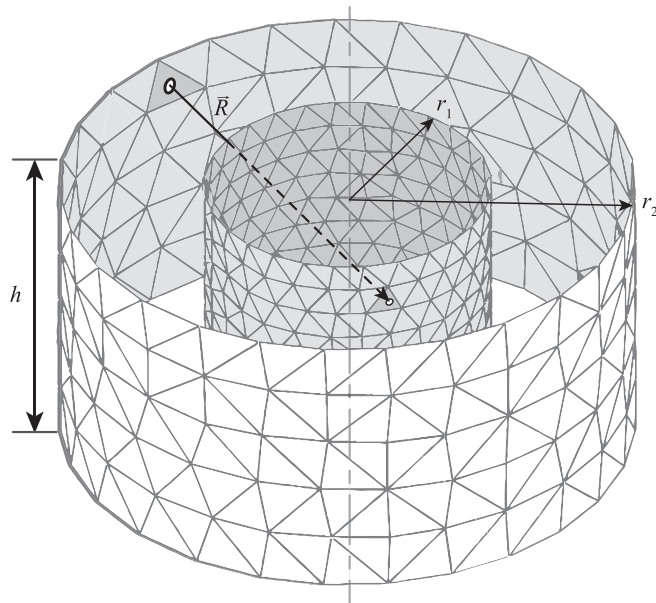
**Table 2**

Comparison of numerical view factors in perpendicular rectangles with the analytical solution.

Z/X	Y/X	Number of Rays	Analytic Solution	Numeric Solution	Error [%]
0.1	0.1	5.4976e+12	7.317119233e-2	7.317125473e-2	8.53e-5
0.1	1.0	7.0369e+13	2.217386709e-1	2.217388368e-1	7.48e-5
0.5	0.1	5.4976e+12	4.653213753e-3	4.653214106e-3	7.59e-6
1.0	1.0	1.7592e+13	5.573419700e-2	5.573420094e-2	7.06e-6
2.0	2.0	4.3981e+12	3.554671952e-2	3.554672686e-2	2.06e-5
4.0	4.0	1.0995e+12	1.929862936e-2	1.929864136e-2	6.22e-5
10.0	10.0	2.1990e+13	7.918234825e-3	7.918234892e-3	8.40e-7
20.0	20.0	4.2950e+11	3.973908672e-3	3.973908778e-3	2.66e-6

**Fig. 10.** Geometrical depiction of the coaxial parallel disks validation case.**Fig. 12.** Geometrical depiction of the concentric spheres validation case.

$R_i$	$R_j$	Number of Rays	Analytic Solution	Numeric Solution	Error [%]
0.2	0.2	1.0370e+13	3.708798216e-2	3.708797017e-2	3.23e-5
0.8	0.8	2.1518e+13	3.071904481e-1	3.071904200e-1	9.15e-6
1.0	1.0	8.3483e+10	3.819660113e-1	3.819660482e-1	6.67e-6
2.0	2.0	2.1519e+13	6.096117968e-1	6.096118609e-1	1.05e-5
5.0	5.0	1.0372e+13	8.190024876e-1	8.190029173e-1	5.25e-5
8.0	8.0	2.1518e+13	8.825685973e-1	8.825691006e-1	5.70e-5
0.1	10.0	2.0950e+12	9.900980392e-1	9.900980380e-1	1.23e-7
10.0	2.0	3.3631e+13	3.958780403e-2	3.958780419e-2	4.07e-7

**Fig. 11.** Geometrical depiction of the concentric cylinders validation case.

$$F_{ij} = \frac{2}{\pi \bar{X} \bar{Y}} \left\{ \ln \left( \frac{(1 + \bar{X}^2)(1 + \bar{Y}^2)}{1 + \bar{X}^2 + \bar{Y}^2} \right)^{1/2} + \bar{X}(1 + \bar{Y}^2)^{1/2} \tan^{-1} \left( \frac{\bar{X}}{(1 + \bar{Y}^2)^{1/2}} \right) + \bar{Y}(1 + \bar{X}^2)^{1/2} \tan^{-1} \left( \frac{\bar{Y}}{(1 + \bar{X}^2)^{1/2}} \right) - \bar{X} \tan^{-1} \bar{X} - \bar{Y} \tan^{-1} \bar{Y} \right\} \quad (17)$$

In this validation case, each specified plate contained 524,288 tessellations per emitting and receiving surface, resulting in over 2.7488e+11 computed rays per configuration. Such discretizations ensured adequate ray coverage across both surfaces, where the spatial coordinates of the initial and terminals points of  $\vec{R}_{ij}$  were obtained from the centroids of  $dA_i$  and  $dA_j$ , respectively. Table 1 highlights the low error obtained in calculating  $F_{ij}$  for various  $\bar{X}$  and  $\bar{Y}$  values in comparison to the analytic solution. It is noted that as the  $\bar{X}$  and  $\bar{Y}$  values increased, the numerical error increased, a direct consequence of enlarged inputted surfaces, i.e., coarser

**Table 4**

Comparison of numerical view factors in concentric, finite right cylinders with the analytical solution.

$r_1/h$	$r_2/h$	Number of Rays	Analytic Solution	Numeric Solution	Error [%]
0.125	0.25	9.9456e+5	4.554342165e-1	4.555764857e-1	3.12e-2
0.25	0.50	1.5294e+8	4.126279102e-1	4.126529479e-1	6.07e-3
0.50	0.75	1.8032e+8	5.443964232e-1	5.444736895e-1	1.42e-2
0.75	1.00	2.3129e+8	6.084371571e-1	6.085189005e-1	1.34e-2
1.00	2.00	6.6535e+7	2.322744982e-1	2.323274504e-1	2.28e-2
2.00	3.00	1.1346e+8	3.007424463e-1	3.007813659e-1	1.29e-2
10.0	32.0	2.5530e+5	8.461822737e-3	8.464075623e-3	2.66e-2

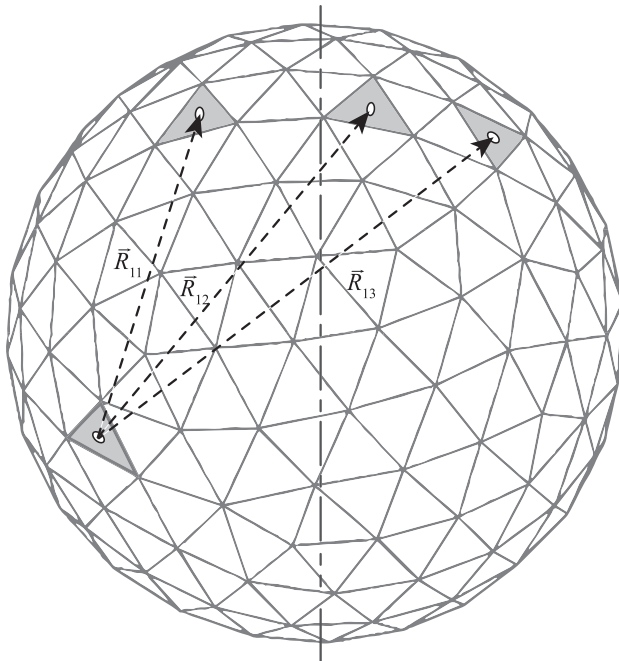


**Fig. 13.** Geometrical depiction of the spherical enclosure validation case.

meshes resulting from an invariant number of rays. Logarithmic convergence to the analytic solution with increasing mesh density is displayed in Fig. 8. The analysis revealed a slope equating to  $-1$ , indicating first-order accuracy.

**3.3.1.2. Perpendicular plates with a differential area.** The next geometrical configuration consists of two perpendicular plates, where one plate was represented as an infinitely small differential area as depicted in Fig. 9. The centroid of the differential area was positioned above the corner of the bottom plate (with lengths  $X$  and  $Y$ ) by some distance  $Z$ . The analytic solution provided by Ref. [46] is

$$F_{ij} = \frac{1}{2\pi} \left\{ \sin^{-1} \frac{X}{(X^2 + Z^2)^{1/2}} - \frac{Z}{(Y^2 + Z^2)^{1/2}} \sin^{-1} \frac{X}{(X^2 + Y^2 + Z^2)^{1/2}} \right\}. \quad (18)$$

**Table 2** compares the numerically obtained solution to the analytical solution for various  $Z/X$  and  $Y/X$  configurations. Similar to Section 3.3.1.1, low percent numerical errors are reported, indicative of adequate ray coverage across both surfaces. It is noted that since the analytical solution required an emitting differential area, to physically represent the differential area within an STL file, a finitely small square grid with dimensions four orders of magnitude smaller than that of the receiving area, was utilized; for example, if  $X$  and  $Y$  were both 1 [mm], the dimensions for the length and width of the differential emitting square area were 1e-4 [mm]. Despite this numeric approximation, good agreement is observed with the analytic solution.

**3.3.1.3. Coaxial parallel disks.** Next, a situation considering curvature in the simplest form is introduced: coaxial parallel discs (see Fig. 10). The analytic solution [45] defines the radii of the two discs as  $r_i$  and  $r_j$ , which are normalized to the distance  $L$  between the two

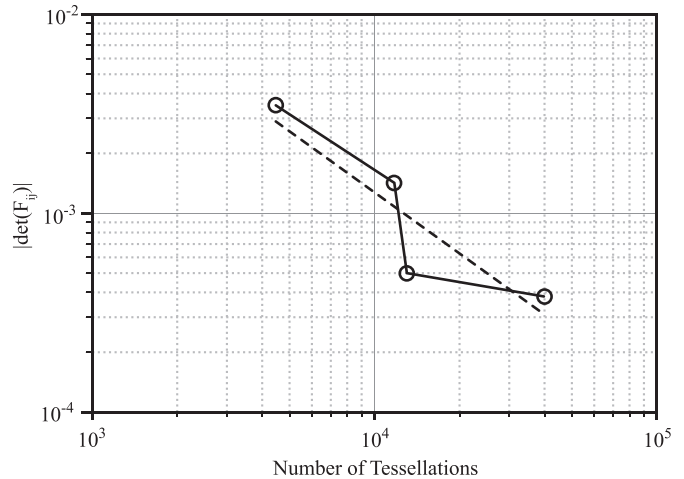


**Fig. 14.** Absolute value of the determinant of the view factor and identity matrices for increasing mesh refinement.

discs such that

$$R_i = \frac{r_i}{L}, \quad R_j = \frac{r_j}{L}. \quad (19)$$

The variable  $S$  is introduced such that

$$S = 1 + \frac{1 + R_j^2}{R_i^2} \quad (20)$$

allowing the view factor to be expressed as

$$F_{ij} = \frac{1}{2} \left\{ S - [S^2 - 4(r_j/r_i)^2]^{1/2} \right\}. \quad (21)$$

As shown in Table 3, the numerical solution was compared to the analytic solution for a range of  $R_i$  and  $R_j$  values. Note the variable number of rays, which is proportional to the number of differential areas. Generally, when  $R_i$  and  $R_j$  increased, which indicated greater emitting and receiving areas or a shorter distance between the discs, the percent error decreased for a comparable number of cast rays.

**3.3.1.4. Concentric, finite right cylinders.** To demonstrate the efficacy of the MT and self-intersection algorithms, which included back-face culling, the view factor for finite, concentric, right cylinders was calculated and compared to the corresponding analytic solution from Ref. [47]. A depiction of the concentric cylinders is shown in Fig. 11. In this configuration,  $h$  is the height of the cylinder,  $r_1$  is the radius of the interior cylinder, and  $r_2$  is the radius of the exterior cylinder. With these variables defined, the radii were normalized to the height such that

$$R_1 = \frac{r_1}{h}, \quad R_2 = \frac{r_2}{h}. \quad (22)$$

The variable  $A$  and  $B$  were introduced such that

$$A = R_2 + R_1, \quad B = R_2 - R_1 \quad (23)$$

allowing for the analytic expression of the view factor to take the form

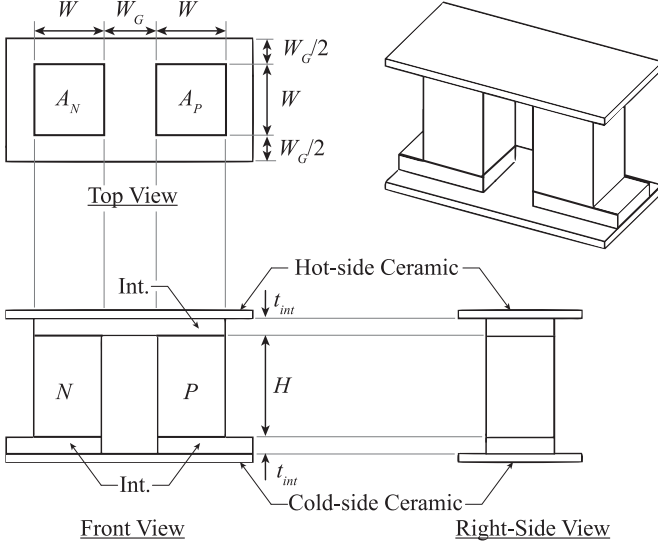


**Fig. 15.** Single-junction thermoelectric generator unit-cell design.

$$F_{ij} = \frac{1}{\pi R_2} \left\{ \frac{1}{2} \left( R_2^2 - R_1^2 - 1 \right) \cos^{-1} \left( \frac{R_1}{R_2} \right) + \pi R_1 - \frac{\pi AB}{2} - 2R_1 \tan^{-1} \left( R_2^2 - R_1^2 \right)^{1/2} + \left( (1+A^2)(1+B^2) \right)^{1/2} \tan^{-1} \left( \frac{(1+A^2)B}{(1+B^2)A} \right)^{1/2} \right\} \quad (24)$$

It is seen in Table 4 that for various  $R_1$  and  $R_2$  values, the large percent error, in comparison to those presented in Section 3.3.1.1 – Section 3.3.1.3, is within acceptable limits. This is attributable to the relatively few numbers of cast rays due to the computational expense of the self-intersection algorithm. As discussed in Section 3.2, the MT and self-intersection algorithms were necessary for an accurate view factor calculation in concentric cylinders because of the internal interference exhibited when a cast ray traversed through one of the convex participating surfaces. However, their implementation necessitated coarse meshes due to the large runtimes from the proportional growth of non-participatory tessellations with mesh refinement. Yet, depending upon the application, numerical errors within one percent for the radiative view factor may be satisfactory. For this reason, the self-intersection methodology was deemed viable.

**3.3.1.5. Concentric spheres.** The final validation case for the proposed view factor methodology was concentric spheres, as described in Fig. 12. The interior sphere has radius  $r_1$  and is completely enclosed by the external sphere of radius  $r_2$ . The analytic solution from Ref. [47] corresponds to total ray absorption by the encapsulating sphere with  $F_{ij} = 1$ .

A single test case was conducted with  $r_1 = 0.50$  [m] and  $r_2 = 1.00$  [m]. A total of  $1.399e+10$  rays were cast, yielding a numeric solution of  $9.998e-1$ . This results in a percent error of 0.12%. As was seen with the finite, right concentric cylinder, the self-intersection algorithm drastically increased the computational time. However, despite this modest discretization, a relatively accurate calculation of the radiative view factor was obtained, demonstrating the efficacy of the hybridized model.

**3.3.1.6. Spherical enclosure.** To supplement the validation of the

calculated view factor within spherical geometries, a single spherical surface (casting internal radiation), was tested after a slight modification to the formulations of this methodology's participating surfaces. As demonstrated in Fig. 13, the view factor within the enclosure should match a value of unity. To check the property of a closed shape, as suggested by Ref. [48], the following relation must hold:

$$\det(\mathbf{F} - \mathbf{I}) = \left| \begin{bmatrix} F_{11} & \cdots & F_{1M} \\ \vdots & \ddots & \vdots \\ F_{N1} & \cdots & F_{NM} \end{bmatrix} - \begin{bmatrix} 1 & \cdots & 0 \\ \vdots & \ddots & \vdots \\ 0 & \cdots & 1 \end{bmatrix} \right| = 0 \quad (25)$$

It is noted that since each emitting surface does not exchange radiation with itself, each  $F_{ii}$  value in the  $\mathbf{F}$  determinant matrix, where  $i$  equates to  $j$ , is zero. Four identical test cases, with differing mesh refinements, were considered. Utilizing a coarse geometry (lower extrema) to cast  $1.998e+7$  rays yielded a determinant equaling  $-3.4488e-3$ , while utilizing a finer mesh (upper extrema, casting  $1.582e+9$  rays) yielded a determinant equating to  $-3.816e-4$ . Fig. 14 depicts the trend of decreasing determinants with increasing mesh refinement. While the memory requirements to compute Equation (25) prevented further (and more accurate surface descriptions), the downward trend exemplified by Fig. 14, along with the proximity of the calculated determinants to zero, give confidence in this work's view factor calculation methodology.

### 3.3.2. Single-junction TEG

In order to further validate the proposed view factor calculation methodology, the results for a single-junction TEG design with varying design parameters were compared with the values reported by Barry et al. [49] (see Fig. 15 for a representation of the device geometry). In this study, the thermoelectric generator design incremented the device height-to-width ratio of the thermoelectric legs,  $H/W$ , the thickness of the interconnector,  $t_{int}$ , and the packing density,  $\varphi$ . The packing density refers to the ratio of the combined cross-sectional areas of the thermoelectric legs to the total cross-sectional area of the exposed hot- and cold-side ceramic plates and is calculated as

$$\varphi = \frac{N(A_p + A_n)}{A_T} \quad (26)$$

where  $N$  represents the number of junctions within the generation design, and  $A_p$  and  $A_n$  represent the cross-sectional area of the p- and n-type thermoelectric materials, respectively. Likewise,  $A_T$  represents the unit cell's total net area. In accordance with Equation (26), as the packing density increases, the gap width separating the p- and n-type thermoelectric legs decreases. To maintain device uniformity, half of the gap width between TE materials,  $W_G$ , was preserved along the perimeter of the generator design; the gap width is expressed, in relation to the packing density, as

$$W_G = \sqrt{\frac{W^2}{\varphi}} - W \quad (27)$$

where  $W$  represents the width of the thermoelectric materials.

While the current methodology utilized different geometry definition procedures and different intersection algorithms, in comparison to those presented in Ref. [49] (MT algorithm versus a point-in-polygon algorithm), good agreement between the two procedures was found. However, it is noted that [49] utilized the total net area of the TEG's ceramic plates, which included the additional areas of the p- and n-type thermoelectric legs and the gap in between, when calculating  $F_{ij}$ , whereas this methodology only considered the ceramic plates' exposed area (see Fig. 1);

**Table 5**

Radiation view factor ( $F_{ij}$ ) values for a single-junction generator design with  $N=1$  and various packing densities ( $\phi$ ), height to width ratios ( $H/W$ ), and interconnector thicknesses ( $t_{int}$ ). The percent numerical difference between the values reported in this work (top row) and the corrected values ( $F_{ijc}$ ) from Ref. [49] (second row) is listed.

View Factor $F_{ij}$												
$\phi$	$H/W$	$t_{int}$ [mm]	0.12500	% Diff.	0.15625	% Diff.	0.18750	% Diff.	0.21875	% Diff.	0.25000	% Diff.
0.1	0.50	4.9135e-1	2.44e-2	4.6837e-1	2.78e-2	4.4737e-1	7.60e-2	4.2768e-1	9.58e-2	4.0921e-1	1.47e-2	
		4.9123e-1		4.6850e-1		4.4703e-1		4.2809e-1		4.0915e-1		
	0.75	4.2171e-1	1.66e-2	4.0364e-1	9.16e-2	3.8720e-1	1.24e-1	3.7145e-1	4.85e-2	3.5659e-1	1.35e-1	
		4.2178e-1		4.0401e-1		3.8768e-1		3.7127e-1		3.5611e-1		
	1.00	3.6651e-1	8.19e-2	3.5218e-1	3.97e-2	3.3863e-1	5.91e-2	3.2581e-1	3.07e-3	3.1368e-1	1.63e-1	
		3.6621e-1		3.5232e-1		3.3843e-1		3.2580e-1		3.1317e-1		
	1.25	3.2160e-1	1.31e-1	3.0986e-1	1.52e-1	2.9871e-1	1.93e-1	2.8813e-1	7.29e-2	2.7807e-1	8.99e-2	
		3.2202e-1		3.0939e-1		2.9929e-1		2.8792e-1		2.7782e-1		
0.3	1.50	2.8444e-1	1.09e-1	2.7468e-1	2.37e-1	2.6539e-1	7.54e-2	2.5653e-1	7.02e-2	2.4808e-1	2.30e-1	
		2.8413e-1		2.7403e-1		2.6519e-1		2.5635e-1		2.4751e-1		
	1.75	2.5325e-1	2.25e-1	2.4503e-1	2.04e-2	2.3719e-1	9.27e-2	2.2969e-1	6.09e-2	2.2252e-1	1.21e-2	
		2.5382e-1		2.4498e-1		2.3741e-1		2.2983e-1		2.2225e-1		
	0.50	2.1943e-1	3.47e-1	2.0131e-1	1.49e-2	1.8586e-1	5.38e-3	1.7209e-1	5.81e-3	1.5979e-1	4.38e-2	
		2.1867e-1		2.0134e-1		1.8585e-1		1.7208e-1		1.5986e-1		
0.5	0.75	1.6831e-1	2.97e-2	1.5674e-1	6.38e-3	1.4628e-1	2.73e-2	1.3678e-1	7.31e-3	1.2813e-1	3.12e-2	
		1.6836e-1		1.5673e-1		1.4632e-1		1.3677e-1		1.2809e-1		
	1.00	1.3403e-1	2.24e-2	1.2585e-1	7.95e-3	1.1836e-1	8.45e-3	1.1148e-1	4.49e-2	1.0515e-1	2.85e-2	
		1.3400e-1		1.2584e-1		1.1837e-1		1.1143e-1		1.0518e-1		
	1.25	1.0931e-1	3.66e-2	1.0328e-1	9.68e-3	9.7714e-2	6.14e-3	9.2556e-2	4.76e-2	8.7769e-2	6.49e-2	
		1.0935e-1		1.0327e-1		9.7720e-2		9.2512e-2		8.7826e-2		
	1.50	9.0769e-2	1.43e-2	8.6197e-2	7.77e-2	8.1940e-2	1.83e-2	7.7746e-2	2.40e-1	7.4262e-2	3.50e-2	
		9.0756e-2		8.6264e-2		8.1925e-2		7.7933e-2		7.4288e-2		
0.7	1.75	7.6475e-2	9.02e-2	7.2923e-2	3.29e-2	6.9596e-2	7.18e-3	6.6478e-2	1.50e-3	6.3548e-2	1.42e-2	
		7.6544e-2		7.2899e-2		6.9601e-2		6.6477e-2		6.3539e-2		
	0.50	1.0006e-1	6.79e-1	8.9740e-2	6.46e-2	8.1451e-2	2.82e-2	7.4340e-2	9.55e-2	6.8190e-2	1.25e-1	
		9.9383e-2		8.9798e-2		8.1474e-2		7.4411e-2		6.8105e-2		
	0.75	7.2239e-2	1.36e-1	6.6215e-2	1.87e-1	6.0925e-2	1.92e-1	5.6290e-2	7.11e-2	5.2204e-2	1.92e-2	
		7.2141e-2		6.6339e-2		6.1042e-2		5.6250e-2		5.2214e-2		
	1.00	5.5173e-2	1.23e-1	5.1180e-2	4.88e-2	4.7580e-2	1.97e-1	4.4326e-2	1.53e-1	4.1418e-2	1.23e-1	
		5.5241e-2		5.1205e-2		4.7674e-2		4.4394e-2		4.1367e-2		
	1.25	4.3572e-2	1.51e-1	4.0774e-2	2.18e-1	3.8220e-2	3.16e-1	3.5883e-2	1.81e-1	3.3739e-2	1.81e-1	
		4.3638e-2		4.0863e-2		3.8341e-2		3.5818e-2		3.3800e-2		
	1.50	3.5264e-2	1.42e-1	3.3225e-2	2.13e-1	3.1345e-2	2.14e-1	2.9609e-2	3.28e-1	2.8004e-2	1.79e-2	
		3.5314e-2		3.3296e-2		3.1278e-2		2.9512e-2		2.7999e-2		
	1.75	2.9092e-2	2.89e-1	2.7560e-2	2.40e-1	2.6136e-2	3.70e-1	2.4813e-2	2.82e-2	2.3580e-2	2.12e-2	
		2.9008e-2		2.7494e-2		2.6233e-2		2.4820e-2		2.3585e-2		
0.9	0.50	4.0348e-2	1.61e-1	3.5930e-2	4.73e-2	3.2515e-2	3.69e-2	2.9621e-2	3.38e-2	2.7134e-2	9.59e-2	
		4.0283e-2		3.5913e-2		3.2503e-2		2.9611e-2		2.7108e-2		
	0.75	2.8044e-2	4.63e-2	2.5648e-2	3.12e-2	2.3591e-2	9.75e-2	2.1802e-2	1.83e-2	2.0228e-2	1.34e-1	
		2.8057e-2		2.5640e-2		2.3568e-2		2.1798e-2		2.0201e-2		
	1.00	2.0933e-2	1.96e-1	1.9360e-2	1.14e-1	1.7990e-2	5.56e-2	1.6782e-2	5.36e-2	1.5705e-2	4.46e-2	
		2.0892e-2		1.9338e-2		1.8000e-2		1.6791e-2		1.5712e-2		
	1.25	1.6281e-2	4.91e-2	1.5172e-2	1.39e-1	1.4199e-2	1.41e-2	1.3334e-2	3.00e-2	1.2557e-2	3.18e-2	
		1.6273e-2		1.5151e-2		1.4201e-2		1.3338e-2		1.2561e-2		
	1.50	1.3034e-2	1.53e-2	1.2221e-2	4.09e-2	1.1497e-2	1.31e-1	1.0851e-2	1.57e-1	1.0268e-2	4.87e-2	
		1.3036e-2		1.2216e-2		1.1482e-2		1.0834e-2		1.0273e-2		
	1.75	1.0657e-2	4.69e-2	1.0053e-2	3.98e-2	9.4985e-3	2.30e-2	9.0000e-3	2.41e-1	8.5488e-3	2.57e-2	
		1.0662e-2		1.0057e-2		9.4963e-3		8.9783e-3		8.5466e-3		
0.5	0.50	9.7472e-3	5.74e-2	8.7240e-3	5.89e-1	7.9185e-3	5.57e-1	7.2275e-3	5.47e-1	6.6281e-3	5.45e-1	
		9.7528e-3		8.6728e-3		7.8745e-3		7.1881e-3		6.5921e-3		
	0.75	6.6560e-3	5.42e-1	6.1225e-3	5.44e-1	5.6541e-3	5.43e-1	5.2396e-3	5.43e-1	4.8703e-3	5.46e-1	
1.00	4.8917e-3	5.39e-1	4.5542e-3	5.42e-1	4.2522e-3	5.42e-1	3.9801e-3	5.44e-1	3.7337e-3	5.45e-1		
	4.8654e-3		4.5296e-3		4.2292e-3		3.9585e-3		3.7134e-3			

**Table 5** (continued)

View Factor $F_{ij}$										
$\phi$	$H/W$	$t_{int}$ [mm]								
		0.12500	% Diff.	0.15625	% Diff.	0.18750	% Diff.	0.21875	% Diff.	
1.25	3.7512e-3	5.40e-1	3.5219e-3	5.44e-1	3.3141e-3	5.41e-1	3.1247e-3	5.42e-1	2.9513e-3	5.44e-1
	3.7310e-3		3.5028e-3		3.2962e-3		3.1078e-3		2.9353e-3	
1.50	2.9661e-3	5.41e-1	2.8023e-3	5.40e-1	2.6528e-3	5.44e-1	2.5153e-3	5.42e-1	2.3884e-3	5.42e-1
	2.9501e-3		2.7872e-3		2.6384e-3		2.5017e-3		2.3755e-3	
1.75	2.4012e-3	5.39e-1	2.2799e-3	5.41e-1	2.1685e-3	5.41e-1	2.0655e-3	5.39e-1	1.9699e-3	5.45e-1
	2.3883e-3		2.2676e-3		2.1568e-3		2.0544e-3		1.9592e-3	

therefore, the following scalar-area correction was applied to the data for an accurate numerical comparison

$$F_{ijc} = F_{ijo} \left[ \frac{(2W + 2W_G)(W + W_G)}{(2W + 2W_G)(W + W_G) - (2W + W_G)W} \right] \quad (28)$$

where  $F_{ijc}$  and  $F_{ijo}$  represent the corrected and original view factor values, from Ref. [49], respectively.

It is also noted that the discretization method of [49]

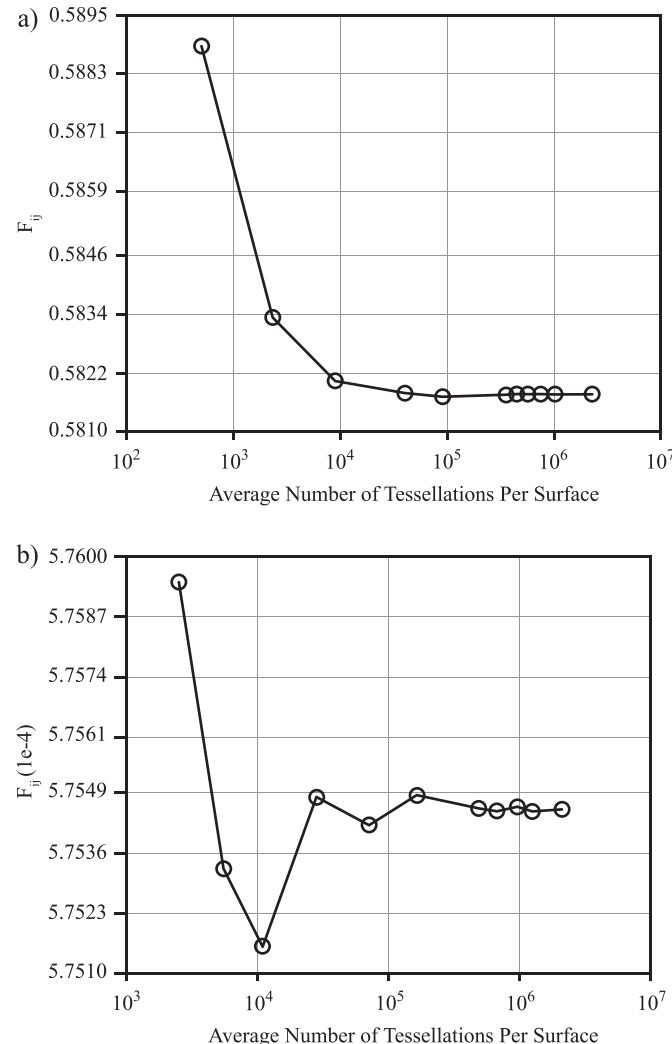


**Fig. 16.** Stabilization of the radiative view factor for increasing mesh refinement in a single-junction generator design with  $N = 1$  for a)  $\phi = 0.1$ ,  $H/W = 0.25$ , and  $t_{int} = 0.125$  [mm] and b)  $\phi = 0.9$ ,  $H/W = 4.00$ , and  $t_{int} = 0.25$  [mm].

incorporated a sub-division of rectangular grids to mesh the ceramic plates, which was based upon the TEG's total cross-sectional area. Since the interface area between the participatory ceramic surfaces and the non-participatory geometries (thermoelectric legs and interconnectors) were modeled within the mesh refinement, overlap could exist between the blocking geometry and the centroidal locations of each grid. This led to potential erroneous coverage of the physically exposed ceramic plates, which could have led to false-positive intersection detections; this modeling mechanism could explain the magnitude of the percent differences between view factors observed in Table 5. Nonetheless, as shown in Table 5, the maximum percent difference between the corrected view factor values for any TEG design was only 0.679%, further validating the numerical methodology proposed in this work.

### 3.3.3. Discretization uncertainty

To determine the effect of successive mesh refinement on the calculated view factors, the grid-convergence index (GCI) was utilized, where the GCI represents the numerical uncertainty due to residual discretization errors [50,51]. The GCI was chosen to estimate numerical uncertainty because it complies with the standard set forth by the American Society of Mechanical Engineers, and it allows for an error estimation when the successive mesh refinements are not integers, as was the case in this study.

The relative GCI between two mesh refinements is defined as

$$GCI = \frac{FS}{r_{21}^p - 1} \left| \frac{F_{ij,2} - F_{ij,1}}{F_{ij,1}} \right| \quad (29)$$

where  $FS$  represents an empirical factor of safety,  $F_{ij,1}$  represents the fine tessellation solution,  $F_{ij,2}$  represents the medium tessellation solution, and  $p$  represents the apparent calculated order. The grid refinement ratio,  $r_{21}$ , is based upon the exponentiated ratio of the average number of tessellations between both participating surfaces and is calculated as

$$r_{21} = \left( \frac{N_1}{N_2} \right)^{\frac{1}{D_s}} \quad (30)$$

where  $D_s$  is the spatial dimensionality and  $N_1$  and  $N_2$  are the average number of tessellations for the fine and medium meshes, respectively. In this case, the average number of emitting and receiving surfaces,  $N_i$  and  $N_j$ , which correspond to the hot- and cold-sides of the thermoelectric generator, are represented in the x-y plane. Thus,  $D_s$  was assigned a value of 2. Furthermore, the empirical factor of safety was assigned a value of 1.25, which is traditionally used when calculating the GCI between three successive computational grids. In this study, when calculating the GCI, each discretization case corresponded to at least a two-fold increase in tessellations between meshes. In reporting the GCI, all values were multiplied by one hundred to give the percent numerical uncertainty.

**Table 6**

Absolute difference between the radiative view factor for increasing mesh refinement in a single-junction generator design with  $N = 1$  and a)  $\phi = 0.1$ ,  $H/W = 0.25$ , and  $t_{int} = 0.125$  [mm] and b)  $\theta = 0.9$ ,  $H/W = 4.00$ , and  $t_{int} = 0.25$  [mm].

Case a)			Case b)		
Avg. Number of Tess.	$F_{ij}$	Difference	Avg. Number of Tess.	$F_{ij}$	Difference
499	5.88865e-1	—	2,527	5.75945e-4	—
2,138	5.83332e-1	5.53e-3	5,538	5.75327e-4	6.18e-7
8,917	5.82037e-1	1.29e-3	11,015	5.75158e-4	1.69e-7
39,952	5.81792e-1	2.45e-4	28,361	5.75481e-4	3.23e-7
90,640	5.81716e-1	7.60e-5	71,586	5.75420e-4	6.10e-8
363,053	5.81758e-1	4.20e-5	165,291	5.75485e-4	6.50e-8
448,829	5.81771e-1	1.30e-5	491,186	5.75457e-4	2.80e-8
567,819	5.81768e-1	3.00e-6	677,544	5.75450e-4	7.00e-9
742,874	5.81770e-1	2.00e-6	969,095	5.75460e-4	1.00e-8
1,012,376	5.81763e-1	7.00e-6	1,263,087	5.75450e-4	1.00e-8
2,278,913	5.81766e-1	3.00e-6	2,121,158	5.75454e-4	4.00e-9

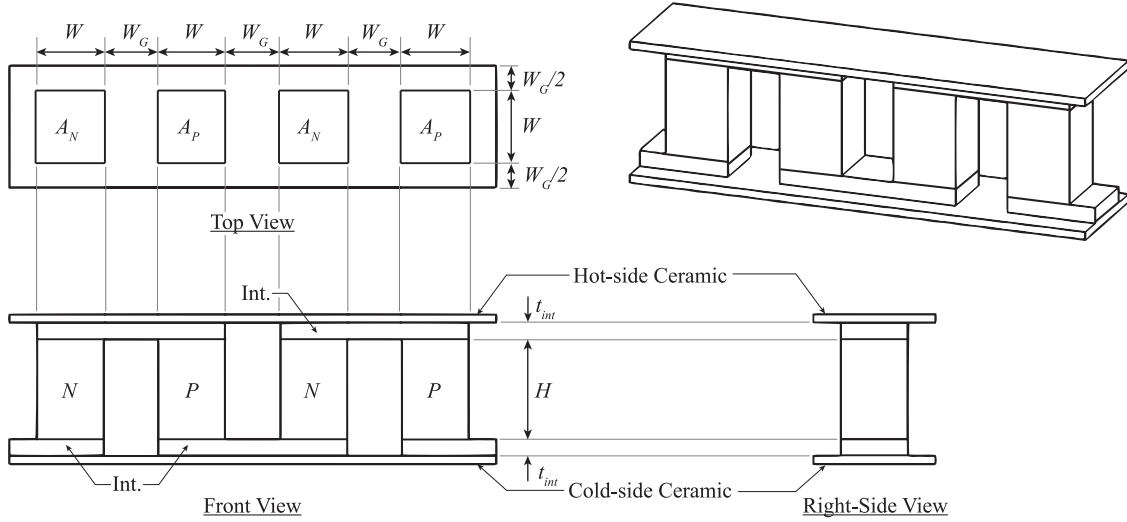


Fig. 17. Double-junction thermoelectric generator unit-cell design.

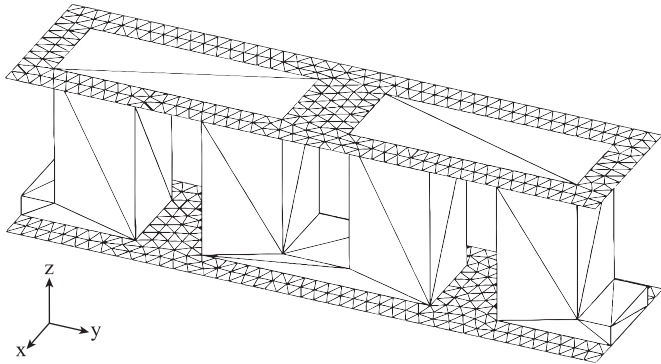


Fig. 18. Example STL input geometry for a double-junction thermoelectric generator unit-cell design.

To further examine the spatial convergence of the calculated view factor with increasing mesh refinement, numerous TEG cases with increasing  $N_i$  and  $N_j$  were created and run through the program. Fig. 16 presents how  $F_{ij}$  changed with an increasing tessellation count, while Table 6 lists the outputted value for  $F_{ij}$  and the difference between the view factor values for the finer and coarser cases. As demonstrated by the incredibly low differences between refined cases, by using a high fidelity model, i.e. the surfaces

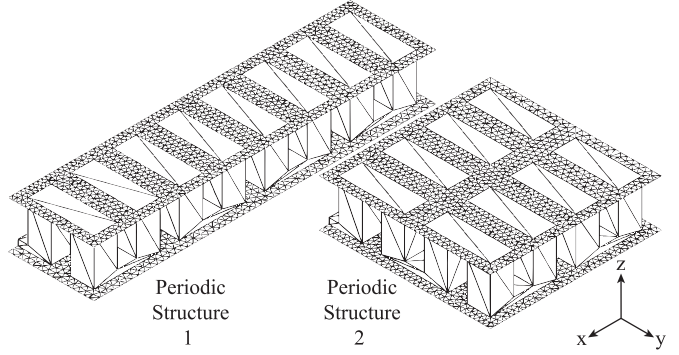


Fig. 19. Example single- and double-junction generator designs with  $N = 8$ .

maintained a large number of tessellations, the view factor stabilized and demonstrated a numerically converged  $F_{ij}$  value.

#### 4. Numerical results for multi-junction TEGs

Two thermoelectric generator designs were considered in this study. The first TEG architecture studied consisted of the same single-junction generator design analyzed in Section 3.3.2 (see Figs. 1 and 15), which repeated its structure along the x-axis as the

**Table 7**

Radiation view factor values for varying geometrical parameters within various single-junction generator designs. The GCI, listed as a percent uncertainty, is within parentheses.

View Factor $F_{ij}$			N				
$\phi$	$H/W$	$t_{int}$ [mm]	N				
			1	2	4	8	16
0.1	0.25	0.12500	5.82e-1 (1.40e-4)	6.37e-1 (4.80e-4)	6.66e-1 (1.05e-2)	6.80e-1 (4.34e-3)	6.88e-1 (7.59e-3)
		0.15625	5.52e-1 (1.16e-4)	6.11e-1 (2.41e-4)	6.42e-1 (1.23e-3)	6.57e-1 (3.92e-3)	6.65e-1 (1.10e-2)
		0.18750	5.24e-1 (4.38e-5)	5.86e-1 (3.59e-4)	6.19e-1 (3.36e-3)	6.35e-1 (4.44e-3)	6.43e-1 (1.40e-2)
		0.21875	4.98e-1 (8.64e-5)	5.63e-1 (3.57e-4)	5.97e-1 (1.91e-3)	6.14e-1 (3.44e-3)	6.23e-1 (6.83e-3)
		0.25000	4.75e-1 (6.30e-4)	5.42e-1 (2.07e-3)	5.77e-1 (1.88e-4)	5.95e-1 (2.55e-5)	6.04e-1 (1.08e-4)
0.1	4.00	0.12500	1.08e-1 (6.16e-5)	1.64e-1 (3.07e-4)	2.05e-1 (5.05e-3)	2.29e-1 (7.18e-3)	2.41e-1 (3.47e-3)
		0.15625	1.06e-1 (1.79e-5)	1.60e-1 (1.12e-4)	2.01e-1 (4.18e-3)	2.25e-1 (7.07e-3)	2.37e-1 (5.74e-3)
		0.18750	1.03e-1 (1.89e-5)	1.57e-1 (1.51e-4)	1.98e-1 (1.51e-3)	2.21e-1 (2.75e-3)	2.32e-1 (6.68e-3)
		0.21875	1.00e-1 (2.01e-6)	1.54e-1 (3.03e-4)	1.94e-1 (4.98e-3)	2.17e-1 (7.54e-3)	2.28e-1 (7.63e-3)
		0.25000	9.88e-2 (8.76e-5)	1.50e-1 (7.20e-5)	1.90e-1 (2.22e-3)	2.13e-1 (3.30e-3)	2.24e-1 (5.50e-3)
0.9	0.25	0.12500	1.61e-2 (9.11e-5)	2.06e-2 (1.59e-4)	2.35e-2 (8.73e-7)	2.49e-2 (1.12e-3)	2.57e-2 (3.19e-6)
		0.15625	1.40e-2 (3.84e-6)	1.77e-2 (2.96e-5)	2.02e-2 (4.57e-7)	2.15e-2 (1.52e-3)	2.21e-2 (6.38e-5)
		0.18750	1.22e-2 (1.69e-6)	1.53e-2 (4.86e-5)	1.75e-2 (1.76e-5)	1.87e-2 (6.60e-4)	1.92e-2 (6.13e-5)
		0.21875	1.08e-2 (2.70e-5)	1.33e-2 (3.34e-6)	1.52e-2 (5.95e-5)	1.63e-2 (7.41e-6)	1.68e-2 (8.86e-5)
		0.25000	9.64e-3 (1.71e-5)	1.19e-2 (1.09e-5)	1.36e-2 (3.49e-5)	1.46e-2 (3.42e-5)	1.51e-2 (5.36e-6)
0.9	4.00	0.12500	6.46e-4 (1.73e-4)	8.24e-3 (8.23e-4)	1.09e-3 (4.42e-3)	1.37e-3 (4.54e-6)	1.56e-3 (8.71e-5)
		0.15625	6.26e-4 (2.03e-4)	7.98e-4 (8.99e-4)	1.06e-3 (5.17e-3)	1.33e-3 (1.43e-5)	1.52e-3 (7.13e-5)
		0.18750	6.08e-4 (1.74e-4)	7.74e-4 (6.32e-4)	1.03e-3 (2.49e-3)	1.29e-3 (2.85e-6)	1.48e-3 (7.96e-5)
		0.21875	5.91e-4 (1.82e-4)	7.52e-4 (5.37e-4)	9.97e-4 (2.52e-3)	1.26e-3 (1.18e-6)	1.44e-3 (8.24e-5)
		0.25000	5.75e-4 (1.67e-4)	7.30e-4 (5.92e-4)	9.69e-4 (1.94e-3)	1.23e-3 (2.70e-6)	1.41e-3 (8.90e-5)

**Table 8**

Radiation view factor values for varying geometrical parameters within various double-junction generator designs. The GCI, listed as a percent uncertainty, is within parentheses.

View Factor $F_{ij}$			N				
$\phi$	$H/W$	$t_{int}$ [mm]	N				
			2	4	6	8	12
0.1	0.25	0.12500	6.02e-1 (9.08e-3)	6.66e-1 (2.16e-4)	6.87e-1 (3.09e-3)	6.98e-1 (1.59e-3)	7.09e-1 (1.25e-3)
		0.15625	5.73e-1 (3.93e-4)	6.42e-1 (3.14e-4)	6.65e-1 (1.16e-3)	6.77e-1 (5.88e-3)	6.89e-1 (2.85e-3)
		0.18750	5.46e-1 (6.50e-4)	6.19e-1 (1.86e-4)	6.43e-1 (1.96e-3)	6.56e-1 (1.38e-3)	6.68e-1 (2.79e-3)
		0.21875	5.21e-1 (1.70e-4)	5.97e-1 (2.27e-4)	6.23e-1 (1.36e-3)	6.36e-1 (5.26e-3)	6.49e-1 (2.70e-3)
		0.25000	4.98e-1 (3.18e-3)	5.77e-1 (1.36e-4)	6.05e-1 (9.53e-4)	6.18e-1 (4.20e-5)	6.32e-1 (1.18e-3)
0.1	4.00	0.12500	1.35e-1 (2.22e-3)	2.10e-1 (8.80e-5)	2.45e-1 (3.06e-3)	2.64e-1 (7.00e-4)	2.83e-1 (4.12e-3)
		0.15625	1.32e-1 (4.01e-4)	2.06e-1 (2.54e-4)	2.40e-1 (8.79e-4)	2.59e-1 (1.57e-3)	2.79e-1 (8.04e-3)
		0.18750	1.30e-1 (2.22e-4)	2.02e-1 (3.55e-4)	2.36e-1 (3.62e-4)	2.55e-1 (2.51e-3)	2.74e-1 (1.55e-3)
		0.21875	1.27e-1 (3.88e-5)	1.99e-1 (2.92e-5)	2.32e-1 (1.45e-3)	2.51e-1 (4.99e-3)	2.70e-1 (3.31e-3)
		0.25000	1.25e-1 (4.30e-6)	1.95e-1 (9.27e-5)	2.28e-1 (2.40e-4)	2.46e-1 (1.82e-3)	2.65e-1 (1.27e-3)
0.9	0.25	0.12500	1.77e-2 (9.42e-4)	2.47e-2 (3.39e-4)	2.73e-2 (4.49e-3)	2.86e-2 (2.55e-3)	2.99e-2 (3.72e-4)
		0.15625	1.54e-2 (1.58e-3)	2.16e-2 (3.16e-4)	2.38e-2 (2.13e-3)	2.49e-2 (1.48e-2)	2.61e-2 (1.49e-4)
		0.18750	1.36e-2 (4.12e-4)	1.90e-2 (4.76e-4)	2.09e-2 (8.93e-4)	2.19e-2 (1.46e-2)	2.29e-2 (1.23e-4)
		0.21875	1.21e-2 (4.01e-4)	1.67e-2 (6.20e-4)	1.84e-2 (2.75e-4)	1.93e-2 (2.50e-2)	2.02e-2 (1.72e-4)
		0.25000	1.09e-2 (1.86e-3)	1.51e-2 (5.50e-4)	1.67e-2 (3.21e-5)	1.75e-2 (3.15e-2)	1.83e-2 (2.55e-5)
0.9	4.00	0.12500	1.09e-3 (8.82e-4)	1.48e-3 (3.67e-3)	1.66e-3 (5.39e-3)	1.77e-3 (3.80e-3)	1.90e-3 (4.86e-5)
		0.15625	1.06e-3 (1.25e-3)	1.44e-3 (6.32e-3)	1.61e-3 (5.48e-3)	1.72e-3 (3.14e-2)	1.85e-3 (3.28e-5)
		0.18750	1.03e-3 (1.25e-3)	1.40e-3 (1.07e-2)	1.57e-3 (5.22e-3)	1.67e-3 (3.15e-2)	1.80e-3 (2.80e-5)
		0.21875	1.01e-3 (1.49e-3)	1.37e-3 (1.33e-2)	1.53e-3 (5.22e-3)	1.67e-3 (2.80e-2)	1.80e-3 (3.58e-5)
		0.25000	9.85e-4 (1.15e-3)	1.33e-3 (5.21e-2)	1.49e-3 (5.31e-3)	1.59e-3 (2.95e-2)	1.71e-3 (3.81e-5)

number of junctions increased through the following range:  $1 \leq N \leq 16$ . Similarly, the second TEG architecture studied consisted of a double-junction generator design that repeated its structure along the x-axis and increased its number of junctions through the following range:  $2 \leq N \leq 16$ ; in this case, the number of junctions increases by a multiple of two. Fig. 17 represents the geometrical parameters that govern the second structure, while Fig. 18 showcases an example double-junction model with the meshed participating surfaces (ceramic plates). To provide a visual comparison between the two periodic structures, sample models

consisting of eight junctions each are represented in Fig. 19.

To study the effect of varying TEG design parameters upon the view factor between the opposing hot- and cold-side ceramic plates, the packing density,  $\phi$ , height-to-width ratio,  $H/W$ , and interconnector thickness,  $t_{int}$ , were varied. To capture the extrema values representative of traditional thermoelectric generator designs, the height-to-width ratios were constrained to a value of either 0.25 or 4.00, while the packing density was fixed to a value of either 0.1 or 0.9; the interconnector thickness was incremented by 0.05625 [mm] through the range of  $0.125 \text{ [mm]} \leq t_{int} \leq 0.25 \text{ [mm]}$ .

Given these design specifications, twenty configurations were created for each multi-junction TEG considered. It is noted that the thermoelectric material width ( $W$ ) was held constant at a value of 1.00 [mm].

**Tables 7 and 8** list the results for the periodic single-junction and double-junction designs, respectively. While it was previously noted that the mesh discretization procedure yielded non-integer refinement ratios, each value reported was calculated using participatory surfaces with no fewer than 500,000 tessellations. As demonstrated, the largest grid-convergence index, for either periodic structure, only amounted to a numeric uncertainty of 0.052%, indicating that the obtained numeric solutions are nearly independent of discretization resolution. Additionally, **Table 9** showcases a decreasing numerical uncertainty with mesh refinement for every TEG design tested. Coupled with the double-precision data types used when calculating the view factor, all potential round-off errors between mathematical steps were alleviated. In this manner, the overall numerical error within the presented view factor data should be relatively negligible.

## 5. Discussion

### 5.1. CPU-GPU runtime comparison

The primary motivation for this proposed methodology is to rectify the intrinsically high computational runtimes associated with resolving the radiative view factor in complex geometries. Therefore, an evaluation of the runtime improvements acquired with GPU-accelerated computing, in comparison to traditional CPU computing, is required.

GPU-acceleration was utilized during the ray-tracing and shadow effect procedures, which constituted the bulk of this method's computational volume. To compare the associated computational gains, graphs of the runtimes for a single-junction design, with  $N = 1$ , running on the CPU and GPU are shown in **Fig. 20**. In these tests, the CPU utilized was the Intel Core i9-9980XE Extreme Edition Processor, while the GPU utilized was the GEFORCE RTX 2080 Ti.

While there exists little difference in runtimes when coarse models (low tessellations) were utilized, there exist massive runtime gains as model fidelity improves for both packing densities. For example, **Fig. 20 a)** showcases a diverging logarithmic time

difference for increasing mesh refinement between the CPU and GPU tests when  $\varphi = 0.1$ . For a low tessellation count (approximately 2,000 tessellations), the decrease in calculation time is 1.3-fold; this is not shown in **Fig. 20 a)**. This in part is due to the time associated with the overhead of data transfer to and from the GPU being on the order of the calculation time. However, as the tessellation count increases to over 1,000,000, the average decrease in computation time is 37.3-fold, with a maximum of 84.8-fold at the highest tessellation count. Further improvement can be gained with increasing tessellation count, which also increases model fidelity. The decrement in computation time is realized due to the embarrassingly parallelizable nature of the calculations for determining the final  $F_{ij}$  value. It is therefore evident that from 20 a), drastic runtime improvements are achievable with GPU-acceleration.

However, as reflected by **Fig. 20 b)**, no direct diverging pattern was observed, but there existed an initial near-order of magnitude difference between runtimes; the computation utilizing GPU-acceleration experienced an average decrease in computation time of 6.2-fold (with a standard deviation of 1.17) in comparison to the CPU-based code. These results are attributable to the lessened dispersion of non-trivial cast radiative rays across the TEG when calculating  $dF_{ij}$ , resulting in the full computation of the MT algorithm and  $dF_{ij}$  value, and thus an increased runtime; a more comprehensive discussion of this trend will be discussed in Section 5.3.

Applying best-fit lines through the CPU and GPU cases shown in **Fig. 21** for  $\varphi = 0.1$  reveals a quantifiable difference between the solution runtimes. The slope of the line describing the computation time versus tessellation count per participating area for CPU-only computations has a value of 2.05, whereas that of the curve describing the GPU-accelerated computations is 1.69. It should be noted that the ordinates of **Fig. 21** are scaled logarithmically and that this seemingly minor variation is indicative of a major difference in computation time. As the tessellation count increases, a proportional increase in computation time is typically expected. That is, based upon the double summation convention used within Equation (8), the number of computations, and cumulative solution time, is quadratic with respect to average tessellation count. The use of GPU-acceleration, which allows for high throughput and high execution density, yields improvements in required computation time comparable to situations of super-linear speedup. However, this marked difference between the CPU and GPU-based

**Table 9**

Spatial convergence study for the radiation view factor in varying geometrical parameters within the single- and double-junction generator designs. The tessellations (Tess.) refer to the average number of discretizations per participating surface.

	Design Parameters	$N = 2$			$N = 8$			$N = 16$		
		Tess.	$F_{ij}$	GCI	Tess.	$F_{ij}$	GCI	Tess.	$F_{ij}$	GCI
Single-Junction Generator Design	$\varphi = 0.1$	28,347	0.6371987	—	17,497	0.6813355	—	34,951	0.6884681	—
	$H/W = 0.25$	727,061	0.6370161	2.5066e-3	113,945	0.6804264	3.0898e-2	144,416	0.6877250	4.5720e-2
	$t_{int} = 0.125$ [mm]	5,190,573	0.6370264	4.8039e-4	824,744	0.6802819	4.3427e-3	923,377	0.6875152	7.5862e-3
	$\varphi = 0.9$	5670	7.296700e-4	—	38,036	1.228921e-3	—	44,038	1.412370e-3	—
	$H/W = 4.00$	116,060	7.300233e-4	4.5207e-3	318,061	1.228675e-3	3.0790e-4	210,331	1.411710e-3	5.3131e-3
	$t_{int} = 0.25$ [mm]	1,187,635	7.300464e-4	5.9240e-4	3,090,361	1.228672e-3	2.6967e-6	2,653,216	1.411651e-3	8.8989e-5
Double-Junction Generator Design	$\varphi = 0.1$	17,942	0.6019617	—	17,821	0.6993057	—	145,796	0.7149603	—
	$H/W = 0.25$	296,834	0.6017303	1.7975e-2	114,433	0.6984707	2.4555e-2	591,606	0.7147815	5.6174e-3
	$t_{int} = 0.125$ [mm]	1,293,670	0.6016875	9.0764e-3	1,538,372	0.6983424	1.5940e-3	1,650,993	0.7147574	1.4142e-3
	$\varphi = 0.9$	27,047	9.854099e-4	—	62,797	1.588271e-3	—	48,439	1.786486e-3	—
	$H/W = 4.00$	114,863	9.853928e-4	2.5487e-3	202,786	1.588493e-3	4.2892e-2	27,0847	1.785766e-3	2.4988e-03
	$t_{int} = 0.25$ [mm]	757,579	9.853819e-4	1.1534e-3	738,337	1.588323e-3	2.9518e-2	1,483,216	1.785732e-3	1.1885e-04

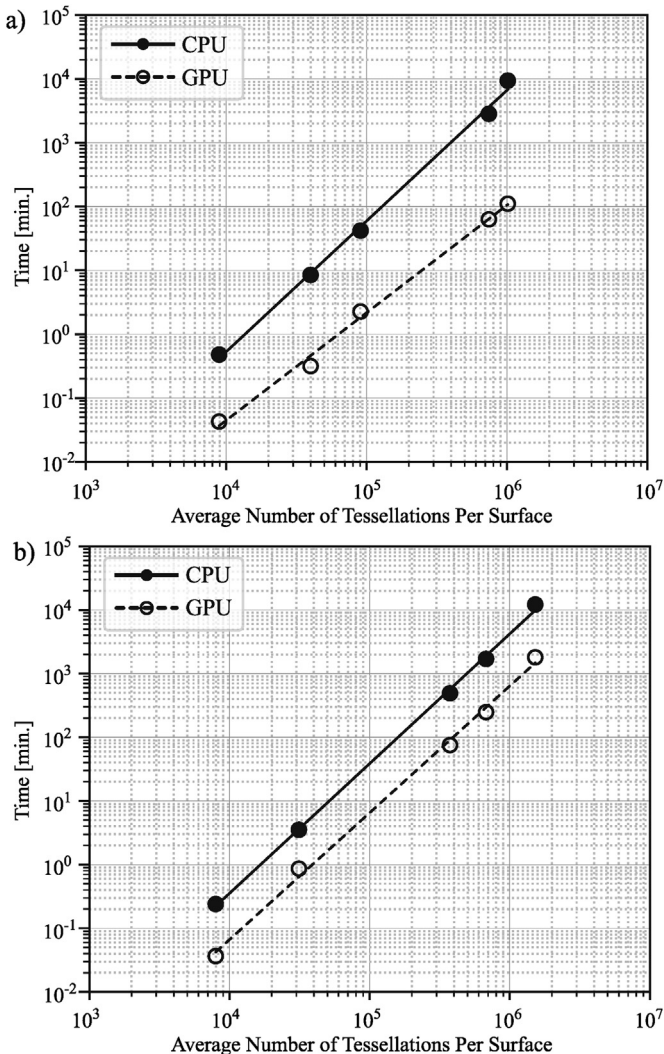


**Fig. 20.** CPU-GPU runtime comparisons in single-junction generator designs with  $N = 1$ ,  $H/W = 1.50$ ,  $t_{int} = 0.125$  [mm] and a)  $\phi = 0.1$  or b)  $\phi = 0.9$ , respectively.

algorithms is absent in the  $\phi = 0.9$  trials, which are characterized by lines with slopes of 2.04 and 1.99, respectively. The slopes being of near equivalent value indicate a near constant achievable decrease in computation time using GPU-accelerated methods. Additionally, for both trials, the computation time for CPU- and GPU-based codes increases to the second power with linearly increasing tessellation count, as is expected.

Finally, it is noted that in situations where the resolution of the shadow effect is substantial or the geometry under consideration requires use of the self-intersection algorithm, runtime improvements are small. For example, employment of the self-intersection procedure for curved geometries drastically increased the number of non-participatory surfaces for the MT algorithm to check, further adding to runtime. Anecdotally, a similar situation was seen when large junction models (greater than 16) were studied or when fine meshes were utilized in the concentric cylinders and spheres analytical tests (all of which maintained a large number of obstructive tessellations). However, given the embarrassingly parallel nature of the problem at hand, it lends itself easily to the ability of multi-GPU acceleration, which could help to overcome this deficiency and serves as an avenue for future work.

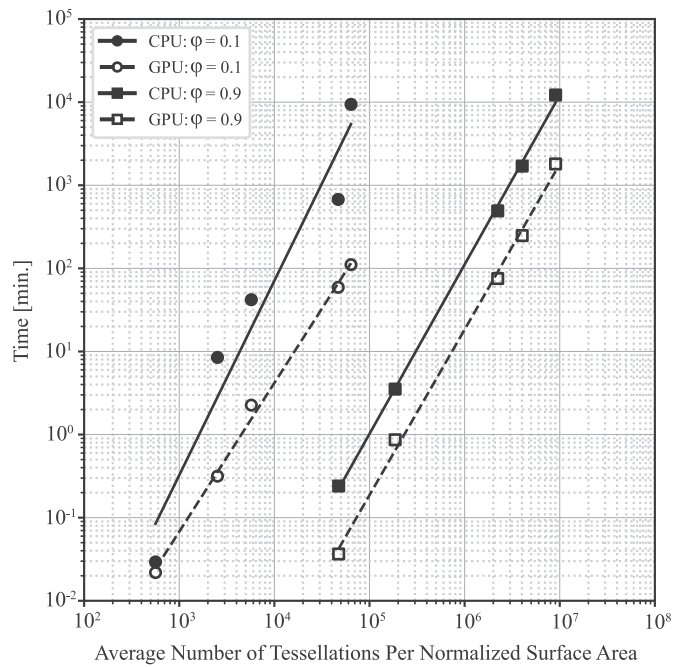


**Fig. 21.** CPU-GPU runtime comparisons in single-junction generator designs with  $N = 1$ ,  $H/W = 1.50$ ,  $t_{int} = 0.125$  [mm], and  $\phi = 0.1$  and  $\phi = 0.9$  in comparison to the average number of tessellations per the average participating surface area.

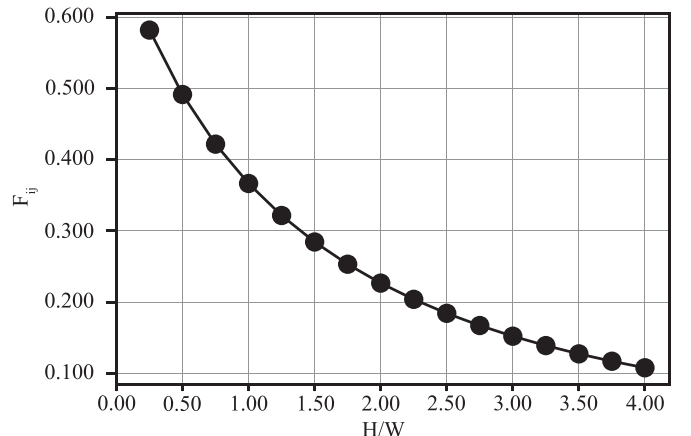


**Fig. 22.** Single-junction generator design with  $N = 1$ ,  $\phi = 0.1$ ,  $t_{int} = 0.125$  [mm], and varying  $H/W$  ratios.

## 5.2. Effect of height/width ( $H/W$ ) and interconnector thickness ( $t_{int}$ )

**Table 5** lists the numerically resolved view factors for numerous single-junction TEG designs, with  $N = 1$ , for varying  $H/W$  and  $t_{int}$  values. Amongst all the independent TEG design variables, the height-to-width ratio and the interconnector thickness demonstrated the most similar effect on  $F_{ij}$ . As demonstrated in Figs. 22 and 23–26, as either  $H/W$  or  $t_{int}$  increased, the radiative view factor monotonically decreased. This trend is attributable to the fact that both design parameters affect the TEG's total height,  $H_T$ . As the generator's total height increased, the radiative ray vector's magnitude increased across the junction, which non-linearly reduced the magnitude of  $F_{ij}$ . Additionally, as the overall TEG height is increased, the polar angles achieved per  $dF_{ij}$  calculation achieved smaller values due to increasingly vertical cast rays, which

contribute to an overall smaller view factor value. **Tables 7 and 8** numerically show the effect of varying either the  $H/W$  ratio or  $t_{int}$  in the multi-junction generator cases, which show the same trend as the single-junction generator design with  $N = 1$ .

It is noted that while varying  $H/W$  or  $t_{int}$  affect the view factor similarly, it is incorrect to assume that the magnitude of  $H_T$  solely determines the magnitude of  $F_{ij}$ . For example, the view factor for a single-junction unit-cell thermoelectric generator design with a packing density of  $\varphi = 0.1$ ,  $H/W = 0.50$ , and  $t_{int} = 0.25$  [mm] obtained a  $H_T = 1.00$ ; likewise, another single-junction unit-cell thermoelectric generator design with  $\varphi = 0.1$  can achieve a  $H_T = 1.00$  with  $H/W = 0.75$  and  $t_{int} = 0.125$  [mm]. However, the two TEG configurations yield different view factors ( $F_{ij} = 0.40915$  and  $0.42178$ ), respectively. **Table 5** further demonstrates this trend via other combinations of  $H/W$  and  $t_{int}$  values to achieve equivalent  $H_T$  values (such as  $H/W = 0.75$  with  $t_{int} = 0.25$  [mm] and  $H/W = 1.00$  with  $t_{int} = 0.125$  [mm], which have  $F_{ij}$  values of  $0.35659$  and  $0.36651$ , respectively). This pattern is apparent in other packing densities, such as when a unit-cell TEG maintains a packing density of  $\varphi = 0.9$  and combinations of  $H/W$  and  $t_{int}$  achieve the same  $H_T$ . For example, a  $H/W$  of  $1.50$  with  $t_{int} = 0.25$  [mm], compared to a design with  $H/W = 1.75$  and  $t_{int} = 0.125$  [mm], yielded  $F_{ij}$  values of  $2.3884\text{e-}3$  and  $2.4012\text{e-}3$ , respectively. These results, which demonstrate larger view factors are achieved when larger TE leg heights are utilized to achieve identical  $H_T$  values, are explained by the geometrical differences between the thermoelectric legs and the interconnectors.

The primary effect of increasing the  $H/W$  ratio on  $F_{ij}$  is the increased magnitude of the cast radiative ray that populates the denominator of the view factor equation; the geometrical differences associated with an increased size of the thermoelectric legs are secondary with respect to their effect on the view factor. On the other hand, geometrical differences associated with an enlarged interconnector play an increased role in determining the view factor. As the interconnector thickness increases, obstructive radiative transfer increases due to the heightened probability of ray-intersection in-between the thermoelectric legs. In this region, tessellations that share an edge with the hot-side interconnector may cast intersected rays when cast to tessellations belonging to the cold-side's perimeter, which further explains why increasing the interconnector thickness can decrease the view factor (besides the enlarged magnitude of the ray vector). Therefore, generators with similar total heights may share similar view factor values, but the values themselves are a function of how the total height was achieved.

### 5.3. Effect of packing density ( $\varphi$ )

An increase in the device's packing density served to decrease the radiative view factor between the hot- and cold-sides of the device. This result is primarily attributed to the decreased exposure area of the ceramic plates resulting from the TEG unicouple

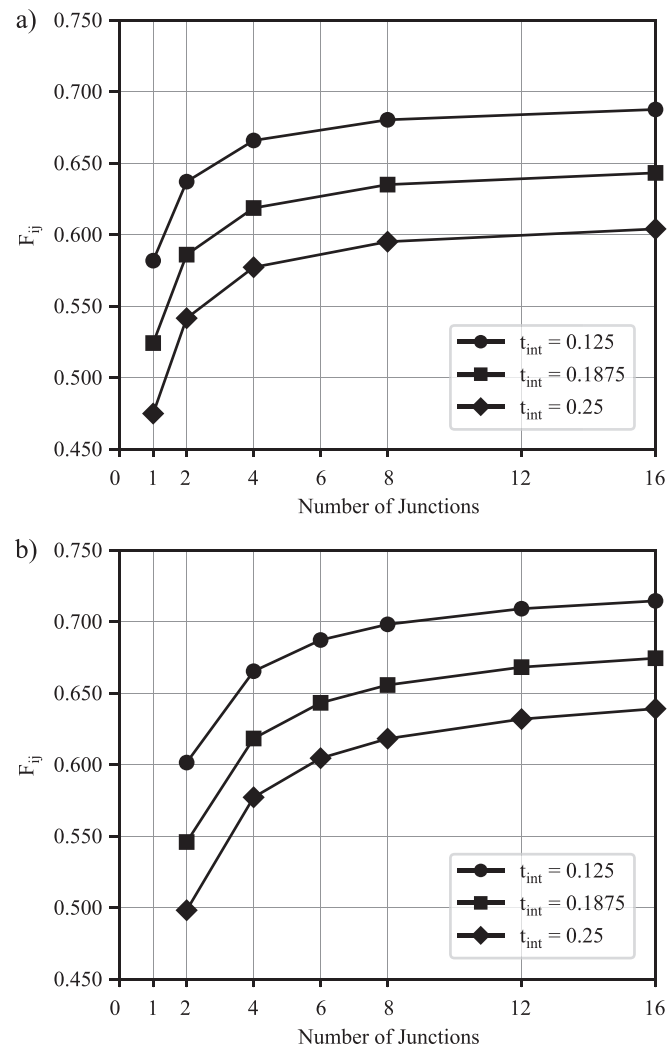


**Fig. 23.** Thermoelectric generator a) single- and b) double-junction designs for  $\varphi = 0.1$  and  $H/W = 0.25$  with varying  $N$  and  $t_{int}$  [mm].

(namely, the interconnector) occupying the majority of the participating surface area. A smaller participatory area decreases the proportion of the ceramic plate capable of radiative transfer, yielding a lesser amount of cast rays that non-trivially participate in the summation of Equation (8), ultimately lowering the overall view factor. **Tables 5, 7 and 8** demonstrate this trend clearly; for example, if the height to width ratio and interconnector thickness are held invariant, the magnitude of  $F_{ij}$  decreases nonlinearly with an increase in packing density.

This nonlinearity is attributed to the nonlinear nature of Equation (8), where for aligned, parallel ceramic plates,  $\theta_i$  and  $\theta_j$  are of

**Table 10**

Absolute difference between the radiative view factor of varying single-junction generator designs with increasing  $N$  for a)  $\varphi = 0.1$ ,  $H/W = 0.25$ , and  $t_{int} = 0.125$  [mm] and b)  $\varphi = 0.1$ ,  $H/W = 4.00$ , and  $t_{int} = 0.25$  [mm].

Case a)			Case b)		
$N$	$F_{ij}$	Absolute Difference	$N$	$F_{ij}$	Absolute Difference
1	0.58177071	-	1	9.8818587e-2	-
2	0.63702645	5.5256e-2	2	0.15038265	5.1564e-2
4	0.66583259	0.28806e-2	4	0.19018161	3.9799e-2
8	0.68028187	0.14449e-2	8	0.21269425	2.2513e-2
16	0.68751517	0.72333e-3	16	0.22425216	1.1558e-2
128	0.69402468	0.65095e-3	128	0.23445169	1.0200e-2

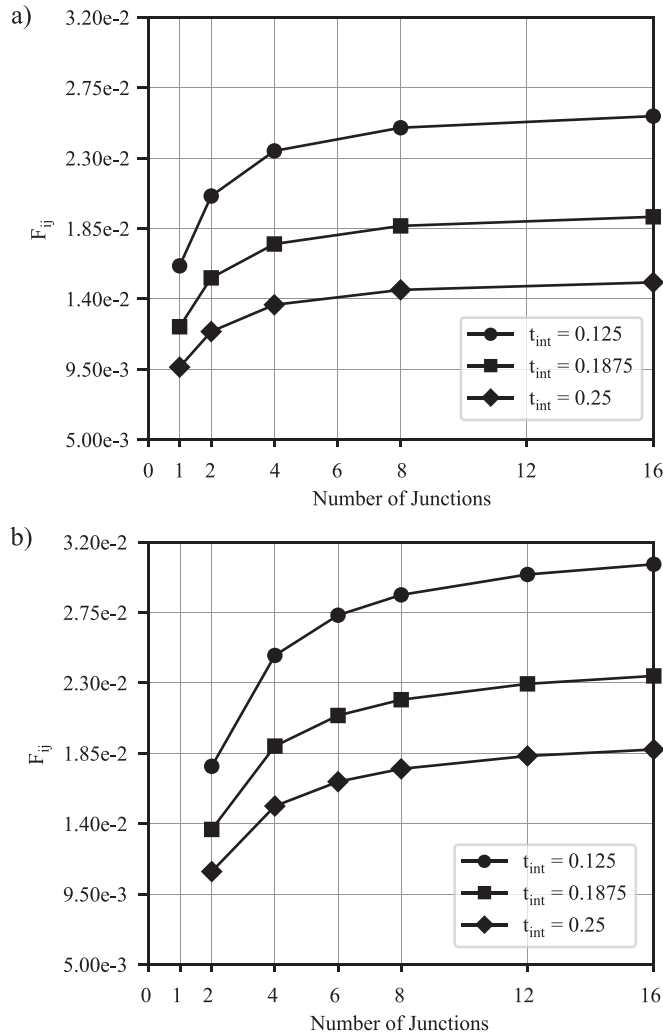


Fig. 24. Thermoelectric generator a) single- and b) double-junction designs for  $\varphi = 0.1$  and  $H/W = 4.00$  with varying  $N$  and  $t_{\text{int}}$  [mm].

equal value when considering a ray existing between two differential areas. Thus, the numerator of Equation (8) is proportional to the cosine-squared value of the polar angle existing between the surface and a ray. High packing density scenarios would result in the average  $\theta_i$  and  $\theta_j$  values, and subsequent cosine-squared thereof, to be smaller and larger (depending upon the choice of  $dA_i$  and  $dA_j$ ), respectively, than those obtained in a lower packing density scenario, leading to an increase in the  $F_{ij}$  value. As  $\varphi$  increases for a fixed  $H/W$  ratio and  $t_{\text{int}}$  value, the maximal value of the magnitude of  $\vec{R}_{ij}$  will decrease, and the average value of the magnitude of  $\vec{R}_{ij}$  will decrease. Although a decrease in the subsequent magnitude of  $\vec{R}_{ij}$  would indicate an increase in  $F_{ij}$  with increasing  $\varphi$ , Tables 7 and 8 show that this is not the case. The contributions from the shadow effect and the nature of the participatory area to the diminution of  $F_{ij}$  must also be considered to explain this behavior.

As the packing density increased, the proportion of the device's volume occupied by non-participatory surfaces increased, leading to a greater chance for ray-triangle intersection, which is substantiated by a decrease in computation time, and will result in a reduced view factor for a set tessellation count. Each unique ray cast from an emitting differential area to a receiving differential

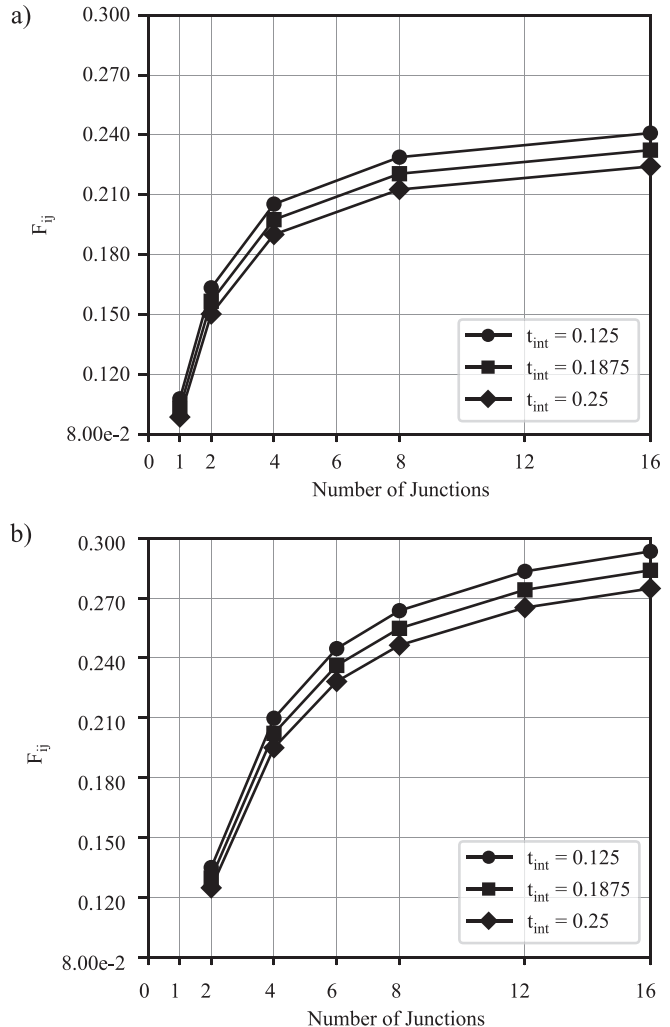


Fig. 25. Thermoelectric generator a) single- and b) double-junction designs for  $\varphi = 0.9$  and  $H/W = 0.25$  with varying  $N$  and  $t_{\text{int}}$  [mm].

area must be checked against every tessellation used to represent the blocking surfaces, as detailed in Fig. 5. If the ray is immediately blocked, its value is set to zero and the MT algorithm ends. If the ray is not, the value of that particular  $dF_{ij}$  is computed, as described by Equation (8). For low packing density devices, given a set differential area density (i.e. number of  $dA$  per unit area), the probability of having a ray intersection is low, and thus the computation time would be expected to be high. Conversely, for a high packing density device, given the same differential area density, the number of rays cast would be far fewer than the low packing density case, and the probability of having a ray intersection would be large. In this situation, the computation time would be expected to be minimal. However, the reverse is seen in Fig. 20 from the previous discussion of computation time. If the average number of tessellations is normalized per the average area of the participating surfaces (i.e. re-expressing Equation (26) for  $A_T$  and then subtracting the area of the interconnector), as shown in Fig. 21, a clearer trend is seen and the empirical runtime discrepancy between packing densities is explained.

As evidenced in Fig. 21, considering a tessellation per participating area value on the order of 47,000 (46,905 for  $\varphi = 0.1$  and 47,416 for  $\varphi = 0.9$ ), the GPU-accelerated computation time is approximately 3780 [s] for  $\varphi = 0.1$ , while for  $\varphi = 0.9$  the

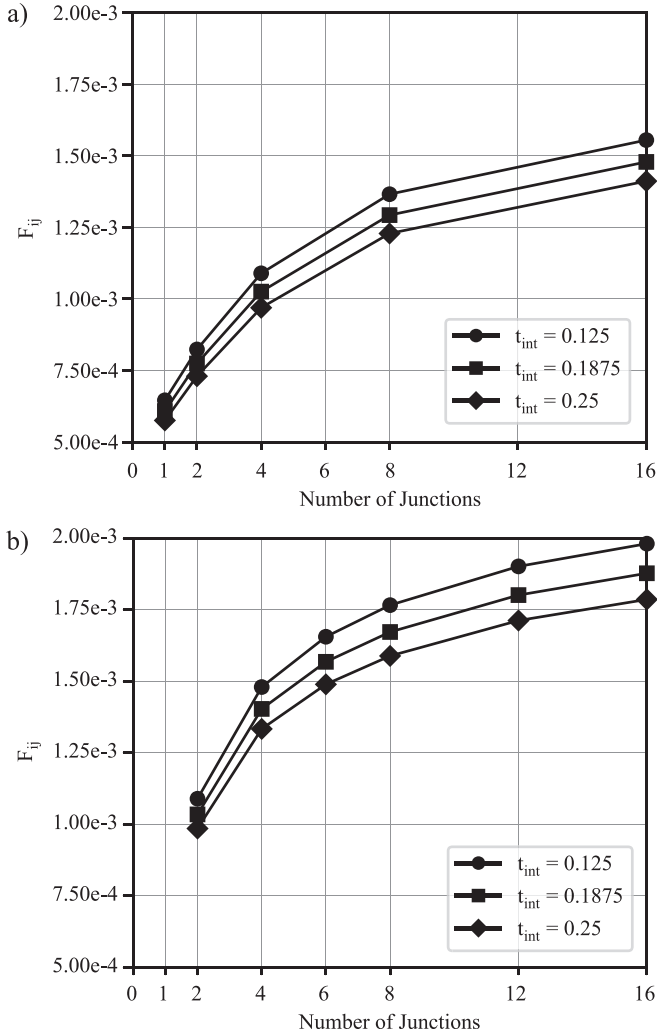


Fig. 26. Thermoelectric generator a) single- and b) double-junction designs for  $\phi = 0.9$  and  $H/W = 4.00$  with varying  $N$  and  $t_{int}$  [mm].

computation time for the same method is approximately 2.2 [s]; this illustrates a 1,700-fold decrease in computation time. At first glance, this appears to directly contradict with the empirical data of Fig. 20. However, one must bear mind the geometrical interpretation of area scaling and how this numerical methodology proceeds during ray-triangle intersection. One can imagine scaling the  $\phi = 0.9$  participatory surfaces to that of  $\phi = 0.1$ 's while holding the tessellation count and internal geometry invariant. In this thought experiment, the tessellation density between both packing density configurations would be equal, yet the  $\phi = 0.9$  case would yield a greater amount of ray-triangle intersections since the TEG's internal geometry occupies a greater device volume than that of the  $\phi = 0.1$  case, resulting in subsequent early breaks during shadow effect resolution procedure and faster runtimes.

However, the above-mentioned situation is not the correct physical interpretation of this work's numerical models. Hence, it is therefore ill-founded to conclude from Fig. 21 that large packing density models yield smaller runtimes. For example, reconsidering the scaled tessellations of 46,905 for  $\phi = 0.1$  and 47,416 for  $\phi = 0.9$ , these values correspond to actual tessellation counts of 742,874 for  $\phi = 0.1$  and 7,972 for  $\phi = 0.9$ , respectively. Thus, given the alleged runtime contradiction between the two cases, it is readily explained due to the near 93-times greater differential areas to

consider in the  $\phi = 0.1$  scenario. Overall, the runtime differences between small and large packing densities, given a set amount of tessellations (without area scaling), are attributable to the relative dispersion of cast rays per  $dA_i$ . In small packing density designs, a lesser number of non-trivial rays that contribute to a  $dF_{ij}$  are computed, whereas in larger packing density designs, a greater number of non-trivial rays are computed, which require completion of the entire MT algorithm and calculation of  $dF_{ij}$  (ultimately leading to greater runtimes). Combining this fact with the contrasting geometric argument that the overall  $F_{ij}$  should increase with increasing packing density due to the interplay of the polar angles and ray magnitude (as discussed in the current and previous sections), it is abundantly clear that the shadow effect plays a very substantial role in dictating the behavior of  $F_{ij}$  with respect to  $\phi$ .

It is also noted that as the packing density increased, the relative effect on  $F_{ij}$  from increasing the device's  $H/W$  or  $t_{int}$  parameters, as shown in Tables 7 and 8, was a monotonic decrement. This suggests that the  $\phi$  value is the dominant parameter in calculating  $F_{ij}$ . Small values of  $F_{ij}$ , characteristic of high packing density TEG designs, reduce the amount of radiative heat transfer between hot- and cold-sides of the device, which can improve the generator's overall efficiency. However, TEG design is multifaceted and many fabricated devices require a large packing density to ensure an ease of manufacturability. Although a limiting case of  $F_{ij}$  being equal to zero as  $\phi$  equals unity would be ideal, it is impractical and unachievable.

#### 5.4. Effect of junction number ( $N$ )

To study the effect of junction number on the radiative view factor, both periodic structures (single- and double-junction generator designs) were analyzed up to  $N = 16$  using the configurations outlined in Figs. 1 and 18. Examples of such multi-junction generator designs are shown in the eight junction configurations (see Fig. 19). To capture the extrema of either configuration, only designs with a packing density of  $\phi = 0.1$  or  $\phi = 0.9$  were considered; likewise, only designs consisting of a  $H/W$  ratio of 0.25 or 4.00 were studied.

Looking to the reported results in Tables 7 and 8, it was found that for constant design parameters, i.e., holding  $\phi$ ,  $H/W$ , and  $t_{int}$  fixed, the radiative view factor behaved asymptotically as the junction number increased. The asymptotic behavior observed in the view factor with increasing junctions and constant design parameters suggested that  $F_{ij}$  within large junction models can be estimated using smaller junction models. To test this hypothesis, a single-junction TEG design with  $N = 128$  was created and compared to similar models as described in Table 7. Table 10 lists the corresponding absolute differences between  $F_{ij}$  in different TEG designs as the junction number increased. As indicated, an increasing junction number yielded a reduced absolute difference in the radiative view factor, further demonstrating the asymptotic behavior between  $F_{ij}$  and  $N$  for constant design parameters.

This trend is explained by the relationship between the exposure area of the TEGs ceramic plates and the number of obstructed radiative rays. As the junction number increases, the total surface area that can participate in radiative transfer increases, but the proportion of the TEG's volume occupied by non participatory geometry (TE legs and interconnectors) similarly increases, which results in a greater proportion of blocked rays. From this perspective, with an increasing  $N$ , the rays that contribute to the overall view factor will increasingly only participate with tessellations in their near vicinity. In other words, a greater proportion of the participatory rays will maintain a large magnitude in the directional vector's z-component, and those rays that jettison outward in diagonal directions will intersect with the TEG's internal geometry. Thus, the view factor of multi-junction TEG designs will

emulate the trends of parallel plate geometries when the  $X/L$  ratio increases. Indeed, a similar asymptotic trend is seen between Figs. 23–26 and the parallel plate view factor plots in Ref. [45].

Furthermore, it is seen that as the packing density, height-to-width ratio, or interconnector thickness increased, the asymptotic behavior, with respect to the view factor, took more junctions to stabilize. This observation is readily explained due to the relative magnitude in the increase in  $F_{ij}$ . Comparing the single-junction TEG designs of  $\phi = 0.1$  and  $\phi = 0.9$ , while holding  $H/W$  and  $t_{int}$  invariant, a decrease in  $F_{ij}$  of over two orders of magnitude is observed. Thus, any change in the geometry more readily affected the view factor's asymptotic behavior when a large packing density was utilized, albeit on a much smaller scale.

### 5.5. Effect of mesh resolution

Determination of an accurate view factor value is highly dependent upon the quality of the surface's tessellations within the part's STL file. This observation is readily seen by the minute oscillations in Fig. 16 b) for the  $F_{ij}$  values of a single-junction TEG. Large packing density designs, in comparison to designs with a small  $\phi$ , appear to maintain a heightened sensitivity to mesh refinement. Yet this numerical sensitivity is apparent for TEGs with small packing densities as well if one looks at comparable decimal places.

The numerical methodology described in this work defines radiative rays via the calculated centroids of each tessellation within the surface's mesh, which play a deciding role when detecting ray-triangle intersections during the MT algorithm. Small changes in centroidal locations after successive mesh refinements, near the TE legs, interconnectors, or any other non-participating surface, can affect the calculated view factor when many significant figures are required. However, while continually decreasing the size of each differential area will improve numerical convergence and obtain more accurate results (more decimal places), doing so is often superfluous when utilizing  $F_{ij}$  in radiative heat transfer calculations; it is often the case that three or four decimal places are sufficient since each order of accuracy gained contributes less to the view factor's magnitude. For example, Table 9 demonstrates how the tessellation number within TEG designs affected the view factor and the corresponding GCI value between coarse and fine mesh cases. While it is shown that finer meshes yielded smaller numerical uncertainties, most  $F_{ij}$  values remained invariant up to the third decimal point after a sufficiently high number of tessellations (20,000–50,000) were utilized.

The view factor's sensitivity to mesh resolution is also apparent in Section 3.3.1.6 when calculating the determinant of the subtracted view factor and identity matrices for a spherical enclosure. Curved surfaces are difficult to approximate with planar surfaces, and achieving an accurate curvature often requires the use of tessellations with large aspect ratios (triangles that significantly deviate from being equilateral). However, doing so is undesirable since the calculated centroidal locations, utilized during the ray-casting procedure, are not representative of the entire tessellation and thus can lead to poor view factor values. For example, the third point in Fig. 14 achieved a much more accurate  $F_{ij}$  value than the second point despite a minimal improvement in tessellation count. The difference between the third point's calculated determinant, and that predicted by the line of best fit, is likely attributable to the tessellations' auspicious orientation and proportional side lengths. Regardless, the results presented in this paper demonstrate that so long as a sufficiently fine and uniform mesh is utilized, this methodology can confidently calculate the view factor in planar and non-planar surfaces.

### 5.6. Implications on device performance

As discussed in the previous sections, TEGs with a low  $H/W$  ratio and small interconnector thickness, low packing densities, and high number of junctions have relatively high  $F_{ij}$  values, exceeding 0.700 in some instances. Reviewing previous RTG designs [2,39], the TEGs typically are comprised of uni-couples with relatively large  $H/W$  ratios, moderate packing densities, and a large numbers of junctions in each module. In regards to the effect of radiation heat transfer within the TEG between the hot- and cold-side ceramics, due to the geometry of these devices, the expected  $F_{ij}$  values are not inconsequential, and play an important role in the analytic and numeric modeling of the devices.

Considering the temperature difference between the two primary participating surfaces can be in the range of 500–700 K for legacy RTG materials, and depending on the thermoelectric materials used (i.e. if the temperature difference is able to be increased), radiation heat transfer can potentially be a substantial, if not dominant, mode of heat transfer, if the interior cavity is operated under a vacuum or an inert back-fill gas. If an interstitial material, such as aerogel, is used within the cavity, thermal leakage from the thermoelectric legs via radiation and convection, as well as radiative and convective heat transfer between the remaining participating surfaces, can be minimized [52]. However, in the absence of light-weight, electrically and thermally insulating packing materials, thermal leakage via the means of radiation heat transfer can substantially reduce device performance [53]. This reduction is due to the fact that the heat source is finite, and if there is substantial thermal leakage via radiation from the hot-to cold-side of the device's internal cavity, the realizable temperature difference across the device will decrease.

With a decreased temperature difference across the p-n junctions, there is a linear decrement in the achievable Seebeck voltage, and correspondingly linear decrement in the produced electric current (if the electrical resistance of the p- and n-legs is not strongly a function of temperature). With a linear decrease in electric current and in temperature, a quadratic decrease in electric power output of the device can be observed. Consequently, a marginal decrease in the temperature difference across the junctions can have substantial ramifications on the ability of the device to produce the desired electrical power, and it will inevitably be operating at a lower efficiency point. Thus, to properly size the legs of TEGs to optimally perform under the expected thermal conditions, all modes of heat transfer must be accurately resolved, including radiation heat transfer.

### 5.7. Implications for numerical modeling

The asymptotic trend between the radiative view factor and the junction number, as discussed in Section 5.4, implies that, depending upon the accuracy needed in the computational model, a smaller junction thermoelectric generator design can accurately approximate  $F_{ij}$  of a larger junction design. This result can lead to major decreases in computational runtime and drastically improve TEG design efficiency, as the data suggests that the largest contributor to runtime is in resolving the shadow effect, which scales with the number of junctions present.

In addition to resolving the view factor within thermoelectric generators, the authors believe that this program is also applicable to other fields where radiation is prevalent. One such example is in calculating  $F_{ij}$  within nuclear pebble bed reactors, such as in the work carried out by Feng et al. [32]. If the reactor utilized a repetitive pattern of spheres within the pebble bed reactor's working model, perhaps a simpler model could estimate the view factor for the entire reactor design, allowing for better insight into how

reactor layout affects the radiative transfer. There are further opportunities in space applications, which rely on SINDA/FLUINT, both of which are CPU-based ray-tracing programs [54,55].

## 6. Conclusions

In this work, a GPU-accelerated ray-tracing method was devised to calculate the radiative view factor between the hot- and cold-sides of two different multi-junction thermoelectric generator designs. The shadow effect, resulting from the generator's thermoelectric legs and interconnectors, was resolved via the Möller-Trumbore ray-triangle intersection algorithm with back-face culling enabled. To calculate the view factor between curved surfaces, a self-intersection partitioning procedure was implemented to prevent erroneous ray-intersection. The use of GPU-accelerated ray-tracing allowed for large decrements in computational runtimes in comparison to CPU-based codes, ultimately allowing for the resolution of  $F_{ij}$  in high-fidelity models. The robustness of the proposed numerical methodology allows for fast and accurate resolution of radiation view factors; however, in situations where self-intersection exists, computational times can become intractable due to additional MT ray-triangle intersection algorithm checks. This issue can be overcome with multi-GPU acceleration, which can capitalize on the embarrassingly parallel nature of the view factor formulation.

The results indicate that in a periodic thermoelectric generator design, the view factor behaves asymptotically with an increasing junction number. Such a trend implies that the view factor of large junction models, representative of working thermoelectric devices, can be approximated using simpler models to save on computational runtime. Determination of the view factor allows for more accurate heat transfer models when radiation is a dominant mode of heat transfer, ultimately aiding in the efficient design and analysis of future thermoelectric generators.

## Credit author statement

Asher J. Hancock: Methodology, Software, Validation, Formal Analysis, Investigation, Data Curation, Writing - Original Draft, Writing - Review & Editing, Visualization, Laura B. Fulton: Methodology, Software, Validation, Investigation, Justin Ying: Methodology, Software, Validation, Investigation, Corey E. Clifford: Validation, Formal Analysis, Writing - Original Draft, Writing - Review & Editing, Shervin Sammak: Resources, Writing - Review & Editing, Matthew M. Barry: Conceptualization, Data Curation, Writing - Original Draft, Writing - Review, & Editing, Supervision, Project Administration, Funding Acquisition.

## Declaration of competing interest

The authors declare that they have no known competing financial interests or personal relationships that could have appeared to influence the work reported in this paper.

## Acknowledgments

Computational resources and support were provided by the Center for Research Computing (CRC) at the University of Pittsburgh. The authors would like to thank Prof. Brian Gleeson of the Mechanical Engineering and Materials Science department at the University of Pittsburgh for providing the local computational resources for prototyping and testing. The authors would also like to thank David J. Garrow for his assistance in editing this manuscript.

## References

- [1] Champier D. Thermoelectric generators: a review of applications. *Energy Convers Manag* 2017;140:167–81.
- [2] Cataldo RL, Bennett GL. US space radioisotope power systems and applications: past, present and future. *Radioisotopes Applications in Physical Sciences*; 2011.
- [3] Cooper PS. Searching for modifications to the exponential radioactive decay law with the Cassini spacecraft. *Astropart Phys* 2009;31(4):267–9.
- [4] Pourkiaei SM, Ahmadi MH, Sadeghzadeh M, Moosavi S, Pour-fayaz F, Chen L, Yazdi MAP, Kumar R. Thermoelectric cooler and thermoelectric generator devices: a review of present and potential applications, modeling and materials. *Energy* 2019;186:115849.
- [5] Gaynor C, Kar KK. Recent advances in thermoelectric materials. *Prog Mater Sci* 2016;83:330–82.
- [6] He W, Zhang G, Zhang X, Ji J, Li G, Zhao X. Recent development and application of thermoelectric generator and cooler. *Appl Energy* 2015;143:125.
- [7] He R, Schierning G, Nielsch K. Thermoelectric devices: a review of devices, architectures, and contact optimization. *Adv Mater Technol* 2018;3(4):1700256.
- [8] He J, Tritt TM. Advances in thermoelectric materials research: looking back and moving forward. *Science* 2017;357(6358):eaak9997.
- [9] Elsheikh MH, Shnawah DA, Sabri MFM, Said SBM, Hassan MH, Bashir MBA, Mohamad M. A review on thermoelectric renewable energy: principle parameters that affect their performance. *Renew Sustain Energy Rev* 2014;30:337–55.
- [10] Tian Z, Lee S, Chen G. A comprehensive review of heat transfer in thermoelectric materials and devices. *Ann Rev Heat Trans* 2014;17.
- [11] Pei Y, Shi X, LaLonde A, Wang H, Chen L, Snyder GJ. Convergence of electronic bands for high performance bulk thermoelectrics. *Nature* 2011;473(7345):66–9.
- [12] Pei Y, Wang H, Gibbs ZM, LaLonde AD, Snyder GJ. Thermopower enhancement in pb 1-x mn x te alloys and its effect on thermoelectric efficiency. *NPG Asia Mater* 2012;4(9):e28–e28.
- [13] Shi X, Chen L, Uher C. Recent advances in high-performance bulk thermoelectric materials. *Int Mater Rev* 2016;61(6):379–415.
- [14] Snyder GJ, Toberer ES. Complex thermoelectric materials. *Materials for sustainable energy: a collection of peer-reviewed Research and review articles from nature publishing group*. World Scientific; 2011. p. 101–10.
- [15] Zhang Q, Wang H, Liu W, Wang H, Yu B, Zhang Q, Tian Z, Ni G, Lee S, Esfarjani K, et al. Enhancement of thermoelectric figure-of-merit by resonant states of aluminium doping in lead selenide. *Energy Environ Sci* 2012;5(1):5246–51.
- [16] Zhu G, Lee H, Lan Y, Wang X, Joshi G, Wang D, Yang J, Vashaei D, Guillet H, Pillitteri A, et al. Increased phonon scattering by nanograins and point defects in nanostructured silicon with a low concentration of germanium. *Phys Rev Lett* 2009;102(19):196803.
- [17] Dresselhaus MS, Chen G, Tang MY, Yang R, Lee H, Wang D, Ren Z, Fleural J-P, Gogna P. New directions for low-dimensional thermoelectric materials. *Adv Mater* 2007;19(8):1043–53.
- [18] Tritt TM. Thermoelectric phenomena, materials, and applications. *Annu Rev Mater Res* 2011;41:433448.
- [19] Szczecz JR, Higgins JM, Jin S. Enhancement of the thermoelectric properties in nanoscale and nanostructured materials. *J Mater Chem* 2011;21(12):4037–55.
- [20] Angrist SW. *Direct energy conversion*. fourth ed. Boston: Allyn and Bacon Inc; 1976.
- [21] Kim HS, Wang T, Liu W, Ren Z. Engineering thermal conductivity for balancing between reliability and performance of bulk thermoelectric generators. *Adv Funct Mater* 2016;26(21):3678–86.
- [22] Jaziri N, Bougahmoura A, Müller J, Mezghani B, Tounsi F, Ismail M. A comprehensive review of thermoelectric generators: technologies and common applications. *Energy Rep* 2019.
- [23] Shu G, Ma X, Tian H, Yang H, Chen T, Li X. Configuration optimization of the segmented modules in an exhaust-based thermoelectric generator for engine waste heat recovery. *Energy* 2018;160:612–24.
- [24] Tian H, Sun X, Jia Q, Liang X, Shu G, Wang X. Comparison and parameter optimization of a segmented thermoelectric generator by using the high temperature exhaust of a diesel engine. *Energy* 2015;84:121–30.
- [25] Argento C, Bouvard D. A ray tracing method for evaluating the radiative heat transfer in porous media. *Int J Heat Mass Tran* 1996;39(15):3175–80.
- [26] Vujičić M, Laverty N, Brown S. View factor calculation using the Monte Carlo method and numerical sensitivity. *Commun Numer Methods Eng* 2006;22(3):197–203.
- [27] Walker T, Xue S-C, Barton G. Numerical determination of radiative view factors using ray tracing. *J Heat Tran* 2010;132(7).
- [28] Cremona P, Billaud Y, Rogaume T, Richard F, Batiot B. Influence of a misalignment of the cone or the sample holder on the view factor with a Monte Carlo approach. *JPhCS* 2018;1107(3):032020.
- [29] Modest MF. *Radiative heat transfer*. Academic press; 2013.
- [30] Mirhosseini M, Rezania A, Rosendahl L. View factor of solar chimneys by Monte Carlo method. *Energy Procedia* 2017;142:513–8.
- [31] Vilchez JA, Muñoz M, Bonilla JM, Planas E. Configuration factors for ground level fireballs with shadowing. *J Loss Prev Process Ind* 2018;51:169–77.

- [32] Feng Y, Han K. An accurate evaluation of geometric view factors for modelling radiative heat transfer in randomly packed beds of equally sized spheres. *Int J Heat Mass Tran* 2012;55(23–24):6374–83.
- [33] Vorre MH, Jensen RL, Le Dréau J. Radiation exchange between persons and surfaces for building energy simulations. *Energy Build* 2015;101:110–21.
- [34] Narayanaswamy A. An analytic expression for radiation view factor between two arbitrarily oriented planar polygons. *Int J Heat Mass Tran* 2015;91:841–7.
- [35] Sönmez FF, Ziar H, Isabella O, Zeman M. Fast and accurate ray-casting-based view factor estimation method for complex geometries. *Sol Energy Mater Sol Cell* 2019;200:109934.
- [36] Walton G. Calculation of obstructed view factors by adaptive integration. USA: US Department of Commerce, Technology Administration, National Institute of Standards and Technology; 2002.
- [37] Kramer S, Gritzki R, Perschke A, Rösler M, Felsmann C. Fully parallel, OpenGL-based computation of obstructed area-to-area view factors. *J Build Perform Simul* 2015;8(4):266–81.
- [38] Mahmood F, Hu Huasi. Obstructed view factor calculations for multiple obstructions in closed cavities. *J Nucl Eng Radiat Sci* 2019;5(1).
- [39] Bennett G, Lombardo J, Hemler R, Silverman G, Whitmore C, Amos W, Johnson E, Schock A, Zocher R, Keenan T, Hagan J. Mission of daring: the general-purpose heat source radioisotope thermoelectric generator. In: 4th international energy conversion engineering conference and exhibit (IECEC); 2006. p. 4096.
- [40] Möller T, Trumbore B. Fast, minimum storage ray-triangle intersection. *J Graph Tool* 1997;2(1):21–8.
- [41] Persson P-O, Strang G. A simple mesh generator in MATLAB. *SIAM Rev* 2004;46(2):329–45.
- [42] Solidworks. Dassault systems SA. 2020. <https://www.solidworks.com>.
- [43] Marschner S, Shirley P. *Fundamentals of computer graphics*. CRC Press; 2015.
- [44] Aparapi Team. Official AMD Aparapi repository. 2020. <https://github.com/aparapi/aparapi>.
- [45] Bergman TL, Incropera FP, DeWitt DP, Lavine AS. *Fundamentals of heat and mass transfer*. John Wiley & Sons; 2011.
- [46] Hottel H, Sarofim A. *Radiative transfer*. McGraw-Hill Series in Mechanical Engineering, McGraw-Hill; 1967.
- [47] Howell JR, Menguc MP, Siegel R. *Thermal radiation heat transfer*. CRC press; 2010.
- [48] Baracu T, Costinas S, Ghiaus C, Badea A, Avram R, Vladulescu F, Jugravescu D. New analytical methodologies for radiative heat transfer in enclosures based on matrix formalism and network analogy. *Appl Therm Eng* 2016;107:1269–86.
- [49] Barry M, Ying J, Durka MJ, Clifford CE, Reddy B, Chyu MK. Numerical solution of radiation view factors within a thermoelectric device. *Energy* 2016;102:427–35.
- [50] Roache PJ. Verification and validation in computational science and engineering, vol. 895; 1998 [Hermosa Albuquerque, NM].
- [51] Celik IB, Ghia U, Roache PJ, Freitas CJ. Procedure for estimation and reporting of uncertainty due to discretization in CFD applications. *J Fluids Eng Trans ASME* 2008;130(7).
- [52] Sakamoto J, Fleuriol J-P, Snyder J, Jones S, Caillat T. Aerogels for thermal insulation of thermoelectric devices. *NASA Tech Briefs* 2006.
- [53] Barry M, Agbim K, Rao P, Clifford C, Reddy BVK, Chyu M. Geometric optimization of thermoelectric elements for maximum efficiency and power output. *Energy* 2016;112:388–407.
- [54] İşik HG, Uygur AB, Ömür C, Solakoglu E. The thermal analysis of a satellite by an in-house computer code based on thermal network method and Monte Carlo ray tracing technique. In: Proceedings of 5th International Conference on Recent Advances in Space Technologies-RAST2011. IEEE; 2011. p. 978–83.
- [55] Andish KK, Eweri MK. Modeling and analysis of the space station freedom active thermal control system radiators using SINDA/Fluent. *Tech Rep SAE Techn Pap* 1992.